Department of Physics and Astronomy

University of Heidelberg

Master thesis

in Physics

submitted by

Malaika Göritz

born in Kaiserslautern, Germany

2024

Implementing a D_1 Grey Molasses for Cooling ^{23}Na in a ^{23}Na-^{39}K Dual Species Ultra Cold Atom Experiment

This Master thesis has been carried out by Malaika Göritz
at the
Kirchhoff Institute for Physics

under the supervision of
Prof. Dr. Markus K. Oberthaler

and
Prof. Dr. Lauriane Chomaz

Abstract

This thesis presents advancements in a dual-species ^{23}Na $-^{39}$ K quantum simulator which is currently under construction. Modifications to the optical setups for both species are detailed.
An offset beat lock for generating light for a high-field imaging scheme needed for potassium in later stages of the experimental sequence is discussed. First, theoretical predictions for offset values at various magnetic field strengths are calculated. Then the implementation of the setup is presented which is informed by these numerical predictions.
Furthermore, the reconstruction of a saturated absorption spectroscopy for simultaneously locking two lasers for sodium is detailed. Finally, the setup of a grey molasses for sodium utilizing the D_1 transition is described. Key molasses parameters and their effects on temperature and atom numbers in a sodium sample are examined. The application of grey molasses during the cooling sequence of the dual-species sample successfully mitigated atom losses, replacing a previously employed microwave evaporation.

Zusammenfassung

In dieser Arberit werden Fortschritte im Bau eines ^{23}Na $-^{39}$ K Dual-Species-Quanten-Simulators präsentiert. Modifikationen der optischen Aufbauten für beide Spezies werden im Detail beschrieben.
Ein Offset Laserlock zur Erzeugung von Licht zum Abbilden von Kalium bei hohen Magnetfeldern wird vorgestellt. Zunächst werden theoretische Vorhersagen für Offset-Werte bei verschiedenen Magnetfeldstärken berechnet. Die Implementierung des Aufbaus, der unter Berücksichtigung dieser numerischen Vorhersagen geplant wurde, wird vorgestellt.
Darüber hinaus wird die Rekonstruktion einer dopplerfreien Sättigungsspektroskopie zum Locken von zwei Lasern für Natrium beschrieben. Schließlich wird der Aufbau einer grauen Molasse für Natrium unter Verwendung des D_1-Übergangs präsentiert. Der Einfluss wichtiger Parameter auf Temperatur und Atomzahlen nach der Melasse wird für den single-species Betrieb diskutiert. Der Einsatz der grauen Molasse während der Kühlsequenz der Dual-Species-Probe konnte durch Ersetzen der zuvor verwendeten Mikrowellenevaporation erfolgreich Atomverluste verringern.

Contents

CHAPTER 1

Introduction

In 1982 Richard Feynman first proposed using quantum systems to simulate large physical systems [1]. His proposition was developed in response to the fact that solving a quantum system numerically with a classical computer requires an amount of time and memory space that scales exponentially with the dimension of the physical system of interest [2]. Historically the computing power of classical computers has increased exponentially according to Moore's law [3]. This trend has recently been slowing down as the physical limits of transistor sizes are reached [4]. Therefore, only a limited amount of physical systems and specifically quantum systems can be investigated with classical computers. Hence quantum simulation has become an effective method for evaluating theoretical models. In this approach, one quantum system is simulated using another quantum system that evolves under a comparable Hamiltonian within a controlled laboratory setting.

There are varying approaches for implementing quantum simulators and computers such as trapped ions [5,6], Rydberg tweezer arrays [7], superconducting circuits [8,9], solid-state spin systems [10, 11] and ultracold atoms. Since the first observation of a Bose-Einstein-Condensate (BEC) [12,13], cold atoms have evolved into a powerful tool for quantum simulation of many body systems. Ultracold atom experiments provide a high degree of control over various important parameters. The interaction strength between particles can be tuned using Feshbach resonances [14, 15] and different potential landscapes can be constructed using light-atom interactions [16, 17]. With a range of cooling and trapping techniques, their temperature and density distribution can be manipulated [18]. With this, a considerable amount of Hamiltonians can be investigated that would not be solvable with classical computation.

Instead of implementing a quantum simulator with a single atomic species, it is possible to apply the same techniques to mixtures of different atomic species. Mixture experiments introduce additional complexities but also enable greater control over various experimental parameters such as inter- and intraspecies interactions, species-specific optical potentials, and phase imprints [19]. This broadens the amount of sim-

ulatable Hamiltonians even further. In this thesis, improvements on the setup of a dual-species ^{23}Na-^{39}K-mixture experiment will be presented.

Combining these two species has several promising applications. Using potassium as impurities, polaron physics can be studied [20–23]. The transition between miscible and immiscible mixtures of the two species can be explored by tuning the inter- and intraspecies interaction strengths [24–27]. Using the less abundant fermionic ^{40}K isotope, dynamical gauge fields could be investigated [28, 29].

In this thesis my contribution to the construction of this sodium-potassium mixture experiment (SoPa) is documented. In Chapter 2, relevant theoretical foundations including Feshbach resonances and dual-species Bose-Einstein condensation are introduced. The development of a high field imaging system for ^{39}K, necessary for working with potassium at the desired magnetic field strengths is presented in Chapter 3. Finally, the setup and implementation of a sodium grey molasses, utilizing the D_1 transition, which is a promising step towards dual-species condensation, is discussed in Chapter 4. The Outlook addresses the milestones that still need to be tackled before the machine can function as a quantum simulator.

CHAPTER 2

SoPa Experiment

In this thesis, changes and additions to several parts of a sodium-potassium experiment (SoPa), which is currently under construction, were made. Before the addition to the potassium setup (see Chapter 3) and the changes and additions to the sodium setup (see Chapter 4) are discussed, a brief overview of the SoPa experiment as a whole is given in this chapter. Some relevant theoretical key concepts, such as Bose-Einstein condensation and Feshbach resonances are addressed.

2.1. SoPa Setup

The SoPa experiment was recently rebuilt by Jan Kilinc and Lilo Höcker. The introductions in this chapter are in largely based on their theses [30] [31]. In the subsequent chapters, my work is presented.

The SoPa experiment consists of two laser tables and one experimental table. Each species has its own laser table where light from several lasers is locked with Saturated Absorption Spectroscopy (SAS), frequency shifted with AOMs and coupled into polarization maintaining optical fibers leading to the experimental table.

In this thesis, changes were made both to the potassium and the sodium laser table. The changes made for potassium are presented in Section 3.2. The new sodium laser table setup is described in Section 4.2. The original laser table setups before the recent modifications can be looked up in Jan Kilinc's PhD thesis [30].

In Figure 2.1, the setup of the experimental table is sketched. Each species is precooled separately in a two-dimensional magneto-optical trap (2D-MOT). Both species then travel to the science chamber where they are captured and form overlapping atom clouds which are cooled and manipulated simultaneously. For a more thorough discussion of the vacuum chamber design and challenges, one can consult Lilo Höcker's thesis [31].

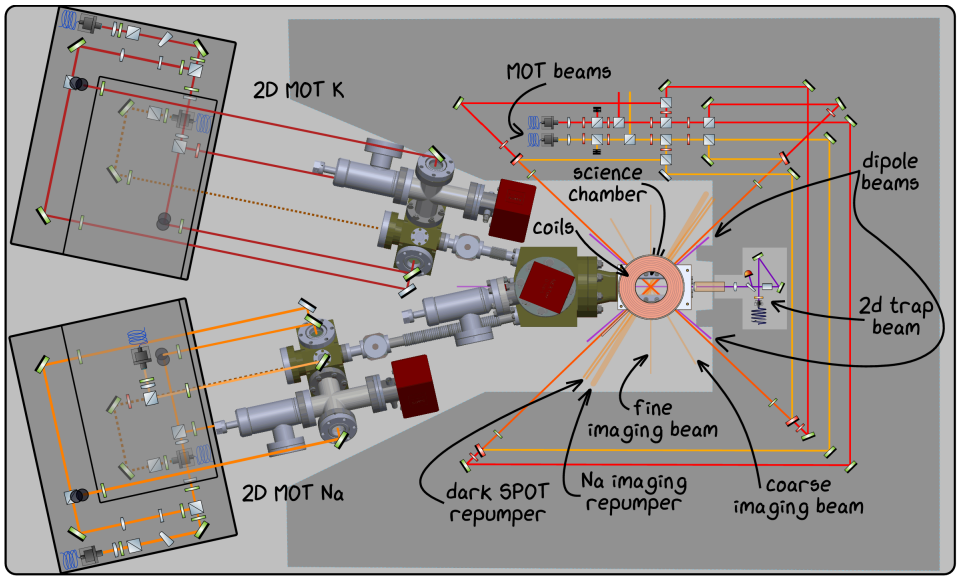

Figure 2.1.: Sketch of the experimental SoPa experimental table setup. Both species are precooled in separate 2D-MOTs and captured in a shared science chamber. Figure taken from [31].

2.2. Cold Atom Theory

This section only briefly addresses some of the most relevant concepts for dual-species cold atom experiments. If one wants to dive deeper into the theory of cold atom experiments, one can consult [32–35] and [18].

2.2.1. Bose-Einstein Condensation

Bose-Einstein condensates (BEC) are a state of matter of bosons which was first postulated by Einstein, based on Bose's description of photon statistics [36, 37]. They form below a critical phase space density

$$\rho = n\lambda_{dB}^3 \leq 2.61 \tag{2.1}$$

where n is the atom number density and $\lambda_{dB} = \sqrt{\frac{2\pi\hbar^2}{mk_BT}}$ is the thermal deBroglie wavelength which depends on the temperature T, the atomic mass m, and the Boltzmann and reduced Planck constants k_B and $\hbar$. Below this critical density, a certain fraction N_0 of the total number of atoms N occupies the ground state. The remaining $N_T = N - N_0$ atoms make up the thermal cloud. The N_0 atoms in the condensed fraction can be described by a shared macroscopic order parameter $\Psi(\mathbf{r}, t)$ [34].

In quantum simulators using cold bosons, BECs are often a crucial step in recreating the Hamiltonians that are being simulated with the machine. Once a cold atom sample has been condensed, a non-linear Schrödinger equation for an interacting Bose gas can be used to describe the dynamics of the condensed fraction. Using a mean field approximation one can derive the Gross-Pitaevskii equation (GPE),

$$i\hbar\frac{\partial}{\partial t}\Psi(\mathbf{r},t) = \left[-\frac{\hbar^2}{2m}\nabla^2 + V(\mathbf{r}) + g|\Psi(\mathbf{r},t)|^2\right]\Psi(\mathbf{r},t) \tag{2.2}$$

where $\Psi(\mathbf{r},t)$ is the order parameter, describing the condensed fraction of the bosons, $V(\mathbf{r})$ is an external potential and g is the coupling strength between the particles with mass m. According to this equation, the time evolution of the order parameter depends on three effects. The first term describes the kinetic energy of the cold atom sample. The second term takes external potentials into account. Lastly, the third term describes the effect of inter-particle interactions [38, 39].

The fact that both the potential $V(\mathbf{r})$ and the coupling strength g can be controlled in ultracold atom experiments, is the reason that they serve as such a powerful tool for quantum simulation. Depending on the potentials that can be shaped and the interaction strengths, that can be reached with a specific machine, a whole range of different Hamiltonians can be implemented and investigated.

2.2.2. Feshbach Resonances

In order to understand how the interaction strength g can be tuned in an atomic sample, one has to be familiar with Feshbach resonances which can be derived using scattering theory. When two bosons in the condensed cloud collide, they experience the interaction potential $V_{int}(\mathbf{R})$ where $\mathbf{R}$ is the separation of the atoms. The incoming particles in this picture are described as plane matterwaves with wave vector k. If $V_{int}(\mathbf{R})$ is isotropic, the outcoming waves, which satisfy the radial Schrödinger equation

$$\left[-\frac{\hbar^2}{2\mu} + V_{int}(R)\right]\phi_l(R) = E\phi_l(R) \tag{2.3}$$

approach

$$\phi_l(R) \to c\frac{\sin(kR - \pi l/2 + \delta_l(E))}{\sqrt{k}}e^{i\delta_l(E)} \tag{2.4}$$

when separating after an interaction ($R \to \infty$). Here c is a normalization constant, μ is the reduced mass, l is the relative angular momentum of the particles, E is the

energy of the separated particles and δ_l is the scattering phase shift that is picked up during a scattering event [15].

In the case of small temperatures where the wave vector k of the incoming atoms approaches zero, one can assume that only s-wave scattering ($l = 0$) contributes. Then the scattering phase shift obeys the simple relationship

$$\tan(\delta_0(E)) = -ka, \tag{2.5}$$

where a is the scattering length. The scattering length is connected to the coupling strength through

$$g = \frac{4\pi\hbar^2 a}{m} \tag{2.6}$$

and can be tuned with an outer magnetic field. When the scattering length is negative, two colliding particles can occupy a bound state of the interaction potential, leading to an attractive interaction. When the scattering length is positive, the bound state has a higher energy than the incoming particles and cannot be occupied. The result is a repulsive interaction. A Feshbach resonance occurs when the energy of the incoming particles is exactly equal to a bound state energy of the interaction potential. Then the scattering length diverges [15] [34].

2.2.3. Mixture Dynamics

For our mixture experiment, the previous discussions have to be expanded to describe two different species interacting with each other. Assuming both species are condensed together with order parameters functions Ψ_1 and Ψ_2 describing each condensate, the coupled GPEs for the dynamics of the system become

$$i\hbar\frac{\partial}{\partial t}\Psi_1 = \left[-\frac{\hbar^2}{2m_1}\nabla^2 + V_1(\mathbf{r}) + g_{11}|\Psi_1|^2 + g_{12}|\Psi_2|^2 \right]\Psi_1 \tag{2.7}$$

$$i\hbar\frac{\partial}{\partial t}\Psi_2 = \left[-\frac{\hbar^2}{2m_2}\nabla^2 + V_2(\mathbf{r}) + g_{22}|\Psi_2|^2 + g_{12}|\Psi_1|^2 \right]\Psi_2 \tag{2.8}$$

Now one has to distinguish between the intraspecies coupling strengths and scattering lengths $g_{11} = 4\pi\hbar^2 a_{11}/m_1$ and $g_{22} = 4\pi\hbar^2 a_{22}/m_2$ and the interspecies coupling strength $g_{12} = g_{21} = 4\pi\hbar^2 a_{21}/\mu$ [25, 34]. In Figure 2.2 the inter- and intraspecies scattering lengths of ^{23}Na and ^{39}K in spin states $|F = 1, m_F = -1\rangle$ are plotted as a function of the outer magnetic field.

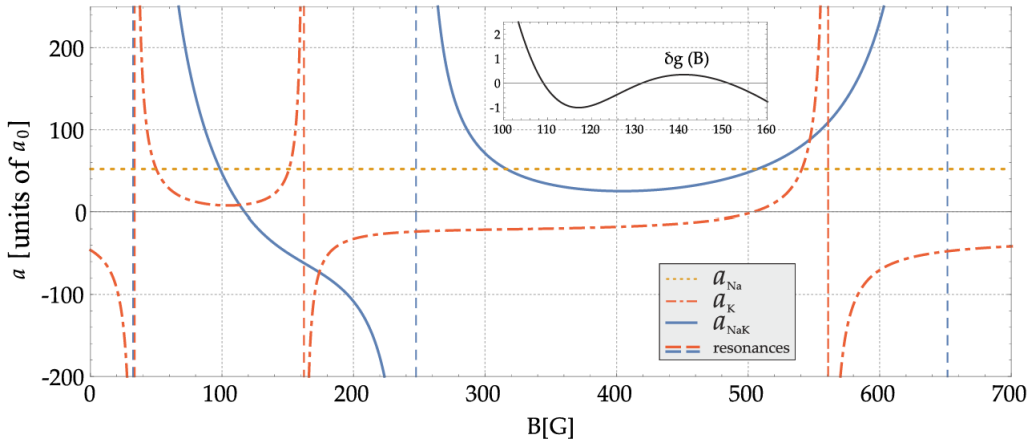

Figure 2.2.: Inter- and intraspecies scattering lenghts of ^{23}Na and ^{39}K in spin states $|1,-1\rangle$ and miscibility parameter δg as a function of magnetic field B. Feshbach resonances are indicated with dashed lines. Figure taken from [40].

Through the coupling strengths g_{ij}, one can define the miscibility parameter

$$\delta g := \frac{g_{12}^2}{g_{11}g_{22}} - 1. \tag{2.9}$$

If $\delta g > 0$, it becomes energetically favorable for the system to demix and separate into potassium and sodium phases [34]. Studying mixing and demixing dynamics of the sodium-potassium sample could be a valuable first benchmark of the quantum simulator, once it is finished. This would require achieving dual-species Bose-Einstein condensation if one wants to understand these dynamics in the framework of the Gross-Pitaevskii mean-field approach. A possibly valuable step in achieving this goal is my implementation of a D_1 grey molasses for sodium which is described in Chapter 4. The additional steps that need to be taken for running the quantum simulator are explained in the Outlook. A numerical simulation of the time evolution of a miscible ($\delta g < 0$) and immiscible ($\delta g > 0$) ^{23}Na-^{39}K-mixture is presented in [30].

CHAPTER 3

Potassium: High Field Imaging

An offset lock consists of an optics setup for producing a beat signal of the master and imaging laser, a lockbox for producing an error signal to lock on, and a a proportional-integral-derivative controller (PID) for reacting to changes in frequency. In this chapter the setup I implemented is presented, including all components, characteristic behaviors and malfunctions, and ways to fix them.

The setup was in large parts adapted from Jan Dreher [41] and Schünemann et al. [42]. Some of the planning for the project had already been carried out before my involvement in the project. Most components used in the project were already ordered but not assembled yet. My contribution to the high field imaging setup included the assembly of the optical and electronic setup. Additionally, the calculations presented in Section 3.1.2 were thoroughly double-checked, and any identified errors were rectified.

3.1. Theory and Motivation

3.1.1. Motivation

As introduced in Chapter 2, inter- and intraspecies interaction strengths quantified via scattering lengths are a key parameter to tune the behavior of a quantum simulator. In the case of our sodium-potassium mixture, they are not only utilized for simulation once the sample has been prepared, but are a crucial part of the cooling process itself. Due to the very strong interspecies interaction at zero magnetic field ($a_{\mathrm{NaK}}(B = 0) = -416a_0$ [40]), big losses can be expected when trying to hold and cool both species in shared traps. This is especially true at later stages of the experimental sequence where densities are large. Indeed these atom losses have been observed and quantified in Jan Kilinc's Doctoral Thesis [30].

To enter the miscibility regime and reduce three-body losses, the magnetic field present must be in a regime where the miscibility parameter δg and the interspecies scattering length a_{NaK} is small. As one can deduce from Figure 2.2, that is roughly the case

for Feshbach fields in the range of 150 G to 170 G. The specific field strength which is optimal for our system has yet to be determined. In any case, going to fields of this magnitude requires a different imaging setup from the one used at zero field due to pronounced effects of Zeeman splitting and shifting.

In this chapter, I will discuss the effects of a magnetic field of $\approx 160\,\mathrm{G}$ on the ^{39}K spectrum and estimate the frequencies needed to image potassium at those field strengths. With the results of this estimation, I will explain the need for and the operation principle of an offset lock. In Chapter 3.2, the implemented optical and electronic offset lock setup is presented.

3.1.2. Zeeman Shifts

The Zeeman effect describes the shifting of energy levels in presence of a magnetic field. An energy level of an atom with total angular momentum F has several Zeeman sublevels which are labeled with the magnetic quantum number m_F. At zero magnetic field, the Zeeman sublevels are degenerate, meaning they have the same energy. When a magnetic field B acts on an atom, the spherical symmetry of the atom Hamiltonian is broken. The degeneracies that resulted from the symmetry are then lifted. Each sublevel experiences shifts of different magnitude due to the outer magnetic field [43]. How the shifting and splitting of the atom spectra due to magnetic fields influences the frequencies needed for our potassium imaging scheme is subject of this section.

The absorption imaging transition currently used for potassium is the D_2 transition at 766.7 nm [44] which has two hyperfine manifolds in the $^2S_{1/2}$ ground state ($F = 1,\ 2$) and four hyperfine manifolds in the $^2P_{3/2}$ excited state ($F' = 0,\ 1,\ 2,\ 3$) (see Figure 3.1 A). For the following discussion a familiarity with the concepts of spin-orbit coupling as well as fine- and hyperfine-splittings will be assumed. For a comprehensive explanation of these topics, one can consult [45] and [43].

For imaging at zero fields only the hyperfine structure has to be taken into account. In the presence of a magnetic field $\mathbf{B}$, both the hyperfine Hamiltonian $\mathbf{H}_{\mathrm{hf}}$ and the Zeeman interaction $\mathbf{H}_{\mathrm{z}}$ influence the potassium energy spectrum and therefore the needed imaging frequencies. The Hamiltonians are given by

$$\mathbf{H}_{\mathrm{hf}} = \frac{A_{\mathrm{hf}}}{\hbar^2}\mathbf{I}\cdot\mathbf{J} + \frac{B_{\mathrm{hf}}}{\hbar^2}\frac{3(\mathbf{I}\cdot\mathbf{J})^2 + \frac{3}{2}(\mathbf{I}\cdot\mathbf{J}) - \mathbf{I}^2\mathbf{J}^2}{2I(2I-1)J(2J-1)} \tag{3.1}$$

$$\text{and } \mathbf{H}_{\mathrm{Z}} = \frac{\mu_B}{\hbar}(g_{\mathrm{J}}\mathbf{J} + g_{\mathrm{I}}\mathbf{I})\cdot\mathbf{B}, \tag{3.2}$$

where $\mathbf{I}$ and $\mathbf{J}$ are the nuclear spin operator and total electronic angular momentum operator respectively, g_{J} is the Landé factor of the electron, g_{I} is the nuclear gyromagnetic factor, μ_B is the Bohr magneton, $\hbar$ the reduced Planck constant and A_{hf} and B_{hf} are the magnetic dipole and electric quadrupole constants [46].

The total Hamiltonian whose eigenfunctions solve the Schrödinger equation for a potassium atom in the presence of a magnetic field is the sum of these two contributions

$$\mathbf{H}_{\mathrm{tot}} = \mathbf{H}_{\mathrm{hf}} + \mathbf{H}_{\mathrm{Z}}. \tag{3.3}$$

For weak magnetic fields, the Zeeman interaction can be treated as a perturbation to the hyperfine solution whose eigenbasis is the $|F, m_F\rangle$ basis. In the case of strong magnetic fields, the Zeeman effect which decouples the angular momenta dominates. The eigenbasis of the Zeeman Hamiltonian are the $|J, I, m_J, m_I\rangle$ or just $|m_J, m_I\rangle$ states [47].

At 160 G especially, the ground state of the potassium D_2 transition is in an intermediate regime where neither of the perturbative approaches yields accurate results. For $J = 1/2$, the Breit-Rabi formula

$$E_{BR}(B) = -\frac{A_{\mathrm{hf}}}{4} + g_I \mu_B m_F B \pm \frac{A_{\mathrm{hf}}(I+1/2)}{2}\left(1 + \frac{4m_F x}{2I+1} + x^2\right)^{1/2} \tag{3.4}$$

$$\text{where } x = \frac{(g_J - g_I)\mu_B}{A_{\mathrm{hf}}(I+1/2)}B \tag{3.5}$$

solves the total Hamiltonian analytically. For other cases, the Hamiltonian has to be diagonalized with numerical methods [48].

To calculate the energy shifts for potassium for different magnetic fields I therefore employed two different methods for the ground state and the $^2\mathrm{P}_{3/2}$ excited state. Since it is true for the ground state that $J = 1/2$, the Breit-Rabi formula can be used to calculate the energy shifts. For the $^2\mathrm{P}_{3/2}$ excited state, the shifts were estimated numerically by diagonalizing the Hamiltonian (Equation (3.3)) using the `numpy.linalg.eigh()` divide and conquer algorithm. It refers to the `_syevd` routine of the Linear Algebra PACKage (LAPACK) which is a standard software library for numerical linear algebra. The Python code used for this can be found in the Appendix. The results of these calculations are plotted in Figure 3.1 B. The energy shifts are given in MHz where I used the linear dispersion relation $E = h \cdot f$ of photons to translate the energy shifts to frequency shifts. This enables the subsequent calculation of imaging light frequencies needed at 160 G.

Before discussing the energy shifts for the high field imaging quantitatively, it is useful to understand the current setup for zero field. As displayed in Figure 3.1 A, the current imaging setup uses both the $|F = 2\rangle \rightarrow |F' = 3\rangle$ and the $|F = 1\rangle \rightarrow |F' = 2\rangle$ transition as a cooling transition and repumping transition respectively. The light is produced by locking a DL pro laser to the crossovers in the ground and excited state and shifting this frequency upwards for the cooler and downwards for the repumper

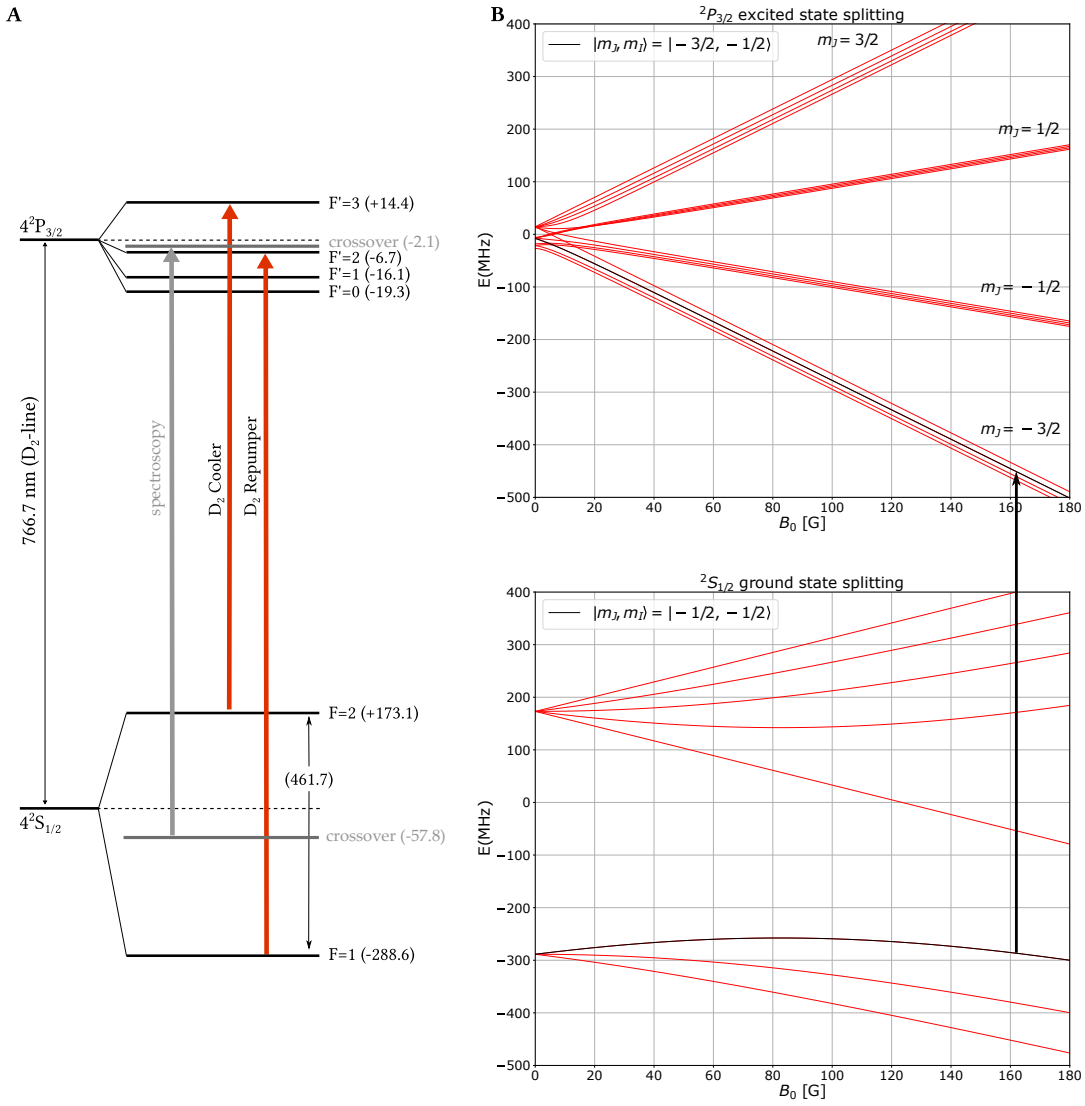

Figure 3.1.: **A)** D_2 transition of ^{39}K. The transitions currently utilized for low field imaging are indicated with red arrows. The lockpoint of the D_2 master laser is indicated in grey. The hyperfine frequency corrections to the fine structure prediction are given in MHz. The potassium hyperfine splitting values were taken from [44] and the figure adopted from [30].
B) Energy spectrum for the ^{39}K $^2S_{1/2}$ ground state and $^2P_{3/2}$ excited state as a function of magnetic field strength B. For nonzero fields, the degeneracy of the manifolds involved in the D_2 transition is lifted. The manifolds being used in the current high field imaging setup are the $|m_J = -1/2, m_I = -1/2\rangle$ and $|m'_J = -3/2, m'_I = -1/2\rangle$ manifolds which are both highlighted in black. A black arrow connecting the manifolds further highlights the transition that is currently planned to be used.

with double passes [30]. For the high field imaging, a tunable offset lock will be employed since the needed shift will be at the larger end of what is easily accessible with double passes as will be calculated below. The details of the optics setup are discussed in 3.2 but for the following calculation, it is necessary to consider that the high field imaging light passes through the cooling light double pass before being coupled into the fine and coarse imaging fibers.

With this knowledge the frequency offset of the high field light can be calculated. All the calculations will use the D_2 transition as a reference and therefore all shifts will be given as detunings in respect to the fine structure prediction $f_{D_2} = 766.7nm$. There are three sources of shifts with respect to this transition. The first shift is introduced by the lockpoint of the D_2 spectroscopy. The master laser is locked to the crossovers which are −57.75 MHz detuned with respect to the ground state and −2.1 MHz detuned with respect to the excited state. The total shift the spectroscopy introduces with respect to the fine structure prediction is therefore $\delta f_{\text{spec}} = 57.75\,\text{MHz} - 2.1\,\text{MHz} = 55.65\,\text{MHz}$ (Figure 3.1 A).
The second shift is added when passing the cooling light double pass. It introduces a shift that is twice the AOM frequency which will be left unchanged during high field imaging operation. The high field imaging frequency will ideally only be tuned via changing the offset instead of making changes to the double pass that is shared with the low field imaging light. Currently, the double pass introduces an offset of $\delta f_{\text{cooler}} = 2 \times 115.5\,\text{MHz} = 231\,\text{MHz}$.

Finally, the hyperfine structure and Zeeman shifts have to be considered. For the high field imaging only the $|F = 1\rangle \rightarrow |F' = 2\rangle$ transition will be employed. In the $|m_J, m_I\rangle$ basis this is the transition between the $|-1/2, -1/2\rangle$ manifold of the ground state and the $|-3/2, -1/2\rangle$ manifold of the excited state which are indicated in black in Figure 3.1 B. Since the Zeeman contribution clearly dominates in the excited state at 160 G, it is safe to assume that the excited state is pure and to a good approximation only the transition to the $|m'_J = -3/2, m'_I = -1/2\rangle$ manifold will be driven with the high field light.

The same can not be said for the ground state. Since the ground state is in an intermediate regime at 160 G, the solution to the Hamiltonian are dressed states which are mixed in the $|m_J, m_I\rangle$ basis. Therefore at 160 G the excited state $|e\rangle = |-3/2, -1/2\rangle$

can decay back into the states

$$|g_-\rangle = \sqrt{p}\,|-1/2,-1/2\rangle + \sqrt{1-p}\,|1/2,-3/2\rangle \tag{3.6}$$

$$\text{and } |g_+\rangle = \sqrt{p}\,|1/2,-3/2\rangle + \sqrt{1-p}\,|-1/2,-1/2\rangle\,. \tag{3.7}$$

To close the cycle, one would therefore ideally not only need light that addresses the $|g_-\rangle \rightarrow |e\rangle$ transition but also light that excites atoms in the $|g_+\rangle$ state. Unfortunately, with the current setup, that is not achievable. Should this pose a significant problem for the imaging quality in the future, it could be worth reconsidering to change the setup such that it includes this second frequency. An alternative setup which addresses this problem can be found in the doctoral thesis of Maurus Hans [49].

The Breit-Rabi and numerical results which are displayed in Figure 3.1 B lead to the following shifts for the ground and excited state: The shift of the $|-1/2,-1/2\rangle$ manifold of the ground state for 160 G is $\delta f_{\mathrm{Z,ground}} = -227.57\,\mathrm{MHz}$ and for the $|-3/2,-1/2\rangle$ manifold of the excited state is $\delta f_{\mathrm{Z,excited}} = -445.4\,\mathrm{MHz}$.

The offset that the high field imaging laser needs to be set to with respect to master laser is therefore

$$\delta f_{\mathrm{offset}} = \delta f_{\mathrm{Z,ground}} - \delta f_{\mathrm{Z,excited}} - \delta f_{\mathrm{spec}} - \delta f_{\mathrm{cooler}} \tag{3.8}$$

$$= -504.48\,\mathrm{MHz} \tag{3.9}$$

In Table 3.1 the offset was calculated for a few other magnetic field values

Table 3.1.: Offset lock detunings needed for different magnetic field strengths

magnetic field strength [G]	offset lock detuning [MHz]
150	–482.87
155	–493.76
160	–504.48
165	–515.04
170	–525.44
180	–545.78

3.1.3. Offset Lock

Generally when locking a laser the main concern is ensuring that it operates at a well defined chosen frequency with high stability. This is done by comparing the laser output to a reference. This reference can be an atomic or molecular transition, an optical cavity, or a second, stable laser which is then called master laser. For an offset lock, the follower laser is locked to a master laser, which in turn itself is stabilized. In our case, the master laser is a DL pro which is stabilized by saturation absorption spectroscopy. It is locked to the ground- and excited state crossovers of the ^{39}K D_2-line (see Figure 3.1). The working principle of saturation absorption spectroscopy is described in Chapter 4.2.2 and the spectroscopy setup currently in use for potassium is described in Jan Kilinc's thesis [30].

In order to lock a laser, an error signal of some sort has to be generated. The error signal should ideally be proportional to the lasers' deviation of a frequency reference. It is an electronic signal that sets a relationship between a voltage and the magnitude of the frequency (or phase) deviation from a reference, which defines the lock point. If the laser frequency is too small, the signal is negative. If it is too large, the signal is positive. At the lock point, the error signal has a zero crossing. An example of an error signal is shown in Figure 3.2.

Since the needed frequency shifts for the high field imaging are not in a range that is nicely accessible with a double pass without significant losses in laserpower (see Table 3.1) and a second laser for high field imaging light was readily available, an offset lock seemed like the most reasonable strategy to implement the high field imaging.

For an offset lock, the error signal is produced by monitoring the beating of the master laser and the follower laser with a photo diode. Beating occurs when two or more coherent and non-orthogonal waves with different frequencies overlap. Due to the superposition principle, the two light fields of the master and follower laser simply sum up when they are superimposed

$$E(t) = a_M e^{i\omega_M t} + a_F e^{i\omega_F t} + \text{c. c.} \tag{3.10}$$

where a_M and a_F describe the amplitudes of the light fields and ω_M and ω_F the frequencies of the the master and follower laser respectively. For simplicity it was assumed that the two beams have the same linear polarization. When measuring this

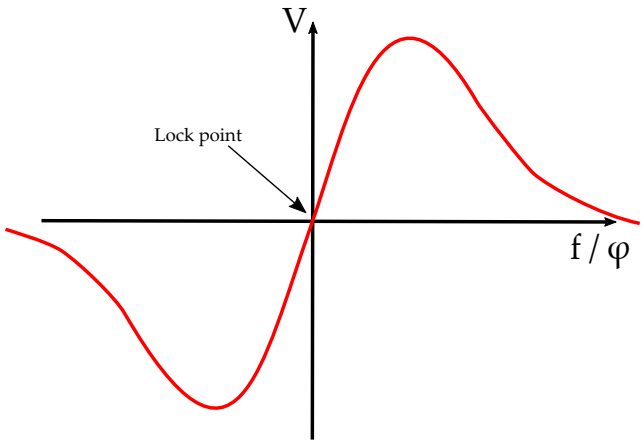

.

Figure 3.2.: Example sketch of an error signal. The zero crossing defines the lockpoint. The capture range in which the lock works well is given by the linear regime. The steeper the slope in the linear regime is, the better the resolution of lock becomes. Then smaller deviations from the lockpoint become detectable. For optimal operation often a tradeoff between capture range and sensitivity has to be found. The figure was adapted from [50]

signal with a photo diode, only the intensity

$$I(t) \propto |E(t)|^2 = |a_M|^2 + |a_F|^2 + a_M a_F^* e^{-i\Delta\omega t} + a_M^* a_F e^{i\Delta\omega t} \tag{3.11}$$

$$= |a_M|^2 + |a_F|^2 + 2\mathfrak{Re}\left(a_M^* a_F e^{i\Delta\omega t}\right) \tag{3.12}$$

$$\propto cos(\Delta\omega t) + \text{DC offset} \tag{3.13}$$

$$\text{where } \Delta\omega = |\omega_M - \omega_F| \tag{3.14}$$

can be detected. Here a_F^* indicates the complex conjugate of a_F. The optics setup used to monitor the beating between the master and follower laser is described in Section Optics Setup.

From this beat signal an error signal can be derived by using a Lockbox. In the Lockbox the voltage $V_P \propto I$ from the photo diode is mixed with itself at a later time. In order to not exceed the bandwidth of the RF components used to process the signal, the beat signal with frequency $\Delta f = \Delta\omega/2\pi$ has to be reduced to a slower frequency. This is done by mixing it with a signal of frequency f_{VCO} produced by a voltage-controlled oscillator (VCO). This has an additional advantage: f_{VCO} depends on the input voltage

V_{tune} applied to the VCO and is therefore tunable. This can later be used to tune the offset lock frequency.

After mixing, the signal has a significantly lower frequency $\delta f = |\Delta f - f_{\text{VCO}}|$. To produce an error signal, this signal is then split into two and later recombined on a phase detector. One part is directly put into the phase detector, whereas the other part is first sent through a delay line and only arrives after a time $\tau = l/c_c$. Here l is the length of the delay line and c_c is the speed of light in the delay line. The phase shift between the two signals introduced by the delay line is then given by

$$\varphi = 2\pi\tau \cdot \delta f. \tag{3.15}$$

The superposition of the two signals

$$V(t) \propto \cos(2\pi\delta f t) \tag{3.16}$$

$$\text{and } V(t+\tau) \propto \cos(2\pi\delta f t + \varphi) \tag{3.17}$$

arriving at the phase detector is therefore

$$V_{\text{detector}} \propto 2\cos(2\pi\delta f t + \varphi) \cdot \cos(\varphi). \tag{3.18}$$

At the phase detector only $\cos(\varphi)$ can be detected since the envelope oscillates at a frequency outside the bandwidth of the detector. The final shape of the error signal is therefore a function of the phase shift φ which depends on the frequency difference Δf between the two lasers [41].

3.2. Setup and Data

3.2.1. Optics Setup

The optics setup was kept as simple as possible. For producing the high field imaging light, an extended cavity diode laser (Toptica DL pro) with an output power of 14.5 mW is used. Its light is split into two paths with a $\lambda/2$-plate and a polarizing beam splitter (PBS). One path receives little power and is used for beat locking the laser to the master laser. The other path which receives most of the power is ultimately used for imaging. For a quantitative measure of laserpowers at every point of the setup, see Table 3.2.

The optics setup for the beat lock is displayed in Figure 3.3. Some D_2 light from the master laser is overlapped with roughly 1 mW of the DL pro light via a 50:50 beam splitter (BS). The beating is monitored with a fiber coupled fast photo diode (Thorlabs DET025AFC/M). To check whether the laser is multimoding, a Fabry-Perot interferometer (Thorlabs SA200-SB) was set up with the second overlapped beam coming from the beam splitter.

Table 3.2.: Laser powers at different points of the high field imaging optics setup

measurement position	laser power [mW]
output high field imaging laser	14.5 ± 0.5
after PBS, offset lock path	0.9 ± 0.1
after PBS, imaging light path	12.3 ± 0.2
before 50:50 BS, master laser	0.44 ± 0.01
after 50:50 BS, master laser	0.21 ± 0.01
after 50:50 BS, imaging laser	0.39 ± 0.01
after fiber to AOMs	7.6 ± 0.2

The remaining 12.3 mW of imaging light are first coupled into a fiber (Figure 3.3 A) which leads it to the low field imaging double paths and AOMs. The setup described in Jan Kilinc's thesis was now slightly modified and extended to include the high field imaging light (Figure 3.4) [30]. Since there was no space to directly couple into the low field imaging fibers which led to the experiment, the high field imaging light has

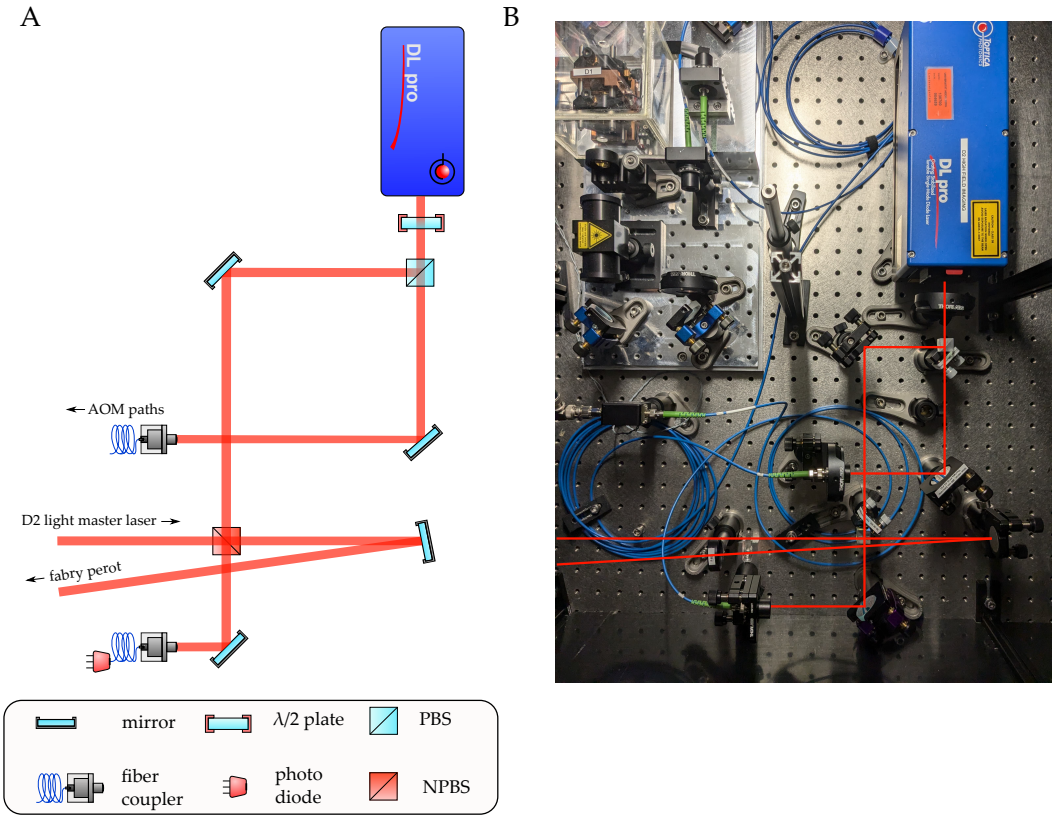

Figure 3.3.: **A)** Schematic of the beat lock optics setup. Imaging light and master laser light are overlapped on a fiber coupled fast photo diode with a 50:50 Beam splitter. The mode structure of both lasers is monitored with a Fabry-Perot interferometer.
B) Picture of the current beat lock setup. The beam paths are indicated with red lines.

to share the cooler and repumper AOM paths with the low field imaging light. The high and low field imaging lights are overlapped with a polarizing beam splitter.

Since the high field imaging could not be used in the experiment yet there are a small handful of things that have not been prioritized and need to be done to finalize the setup. Three shutters have to be built in to make it possible to differentiate between high field or low field operation. One shutter has to block the light coming from the high field imaging for low field imaging operation. Another one has to block the low field imaging light for high field operation. The third one has to be put in the repumper AOM path and has to close during high field imaging operation since only one frequency is desired for the proposed imaging scheme (see Section 3.1.2). When

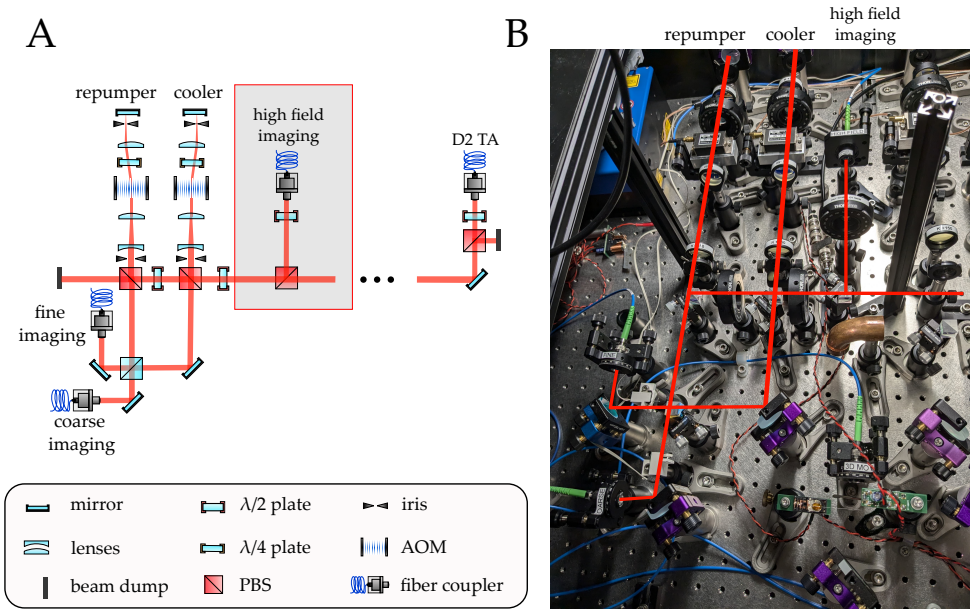

Figure 3.4.: **A)** Schematic of the shared high and low field imaging double passes. The grey box indicates the components that were added to include the high field imaging. For low field imaging both cooler and repumper paths are used. For the high field imaging, only light from the cooler path should be coupled into the imaging fibers that go to the experiment table.
B) Picture of the potassium imaging AOM paths. The red lines indicate the beam paths.

the shutters are placed, the experiment control has to be changed such that the imaging sequence includes different cases for high field and low field imaging where the shutters open and close appropriately.

3.2.2. Lockbox

The design of the lockbox was inspired by a similar setup by Jan Dreher [41]. The purpose of the lockbox is to produce an error signal which later can be locked on with a PID. The setup is sketched in Figure 3.5. The list of parts is given in Table 3.3.

As addressed in Section 3.1.3, there are two main processes that have to happen in the lockbox. The beat signal has to be down-converted by mixing it with a signal produced by a VCO and afterwards overlapped with itself at different points in time by using a delay line. In the following, the processing of the signal is described step by step.

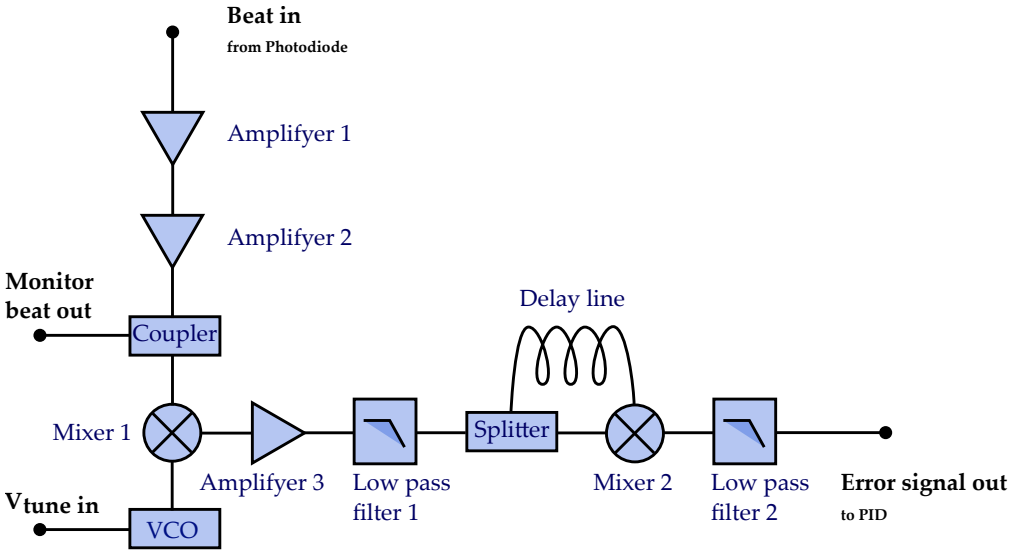

Figure 3.5.: Schematics containing all RF components of the Lockbox.

Table 3.3.: Components of the lockbox, listed in the order that the signal passes through them.

Component	model number
Amplifyer 1, 2	ZX60-3018G-S+
Coupler	ZDFC-15-5-S
Mixer 1	ZFM-15-S+
VCO	ZX95-850W-S+
Amplifyer 3	ZFL-500HLN+
Low Pass Filter 1	SLP-450+
Splitter	SFSC-2-2-S+
Mixer 2	ZEM-2B+
Low Pass Filter 2	SLP-5

The beat signal coming from the photo diode (see Figure 3.3) is amplified via amplifier 1 and 2 from $\approx -35\,\mathrm{dBm}$ to $\approx -13\,\mathrm{dBm}$. With the coupler, 2% of the beat signal is coupled out in order to be able to monitor the offset lock shift with e.g. a frequency counter. If the laser is multimoding, the beat signal will not appear as a proper peak on a spectrum analyzer but rather as a broad hill that spans over a range of $50\,\mathrm{MHz}$.

Mixing the beat with a signal of another frequency produces a carrier, sum- and difference frequency. Since the VCO does not only produce a signal with one mode but rather a signal with a dominant mode and some higher orders, many new modes are introduced after the first mixer. Since we are only interested in the difference frequency of the beat with the dominant mode of the VCO, a low pass filter suppresses the other modes. An example of the spectrum after low pass filter 1 and before the splitter is plotted in Figure 3.6. Here, one can see that the higher orders introduced by the VCO are still present, but strongly suppressed (by >25 dB).

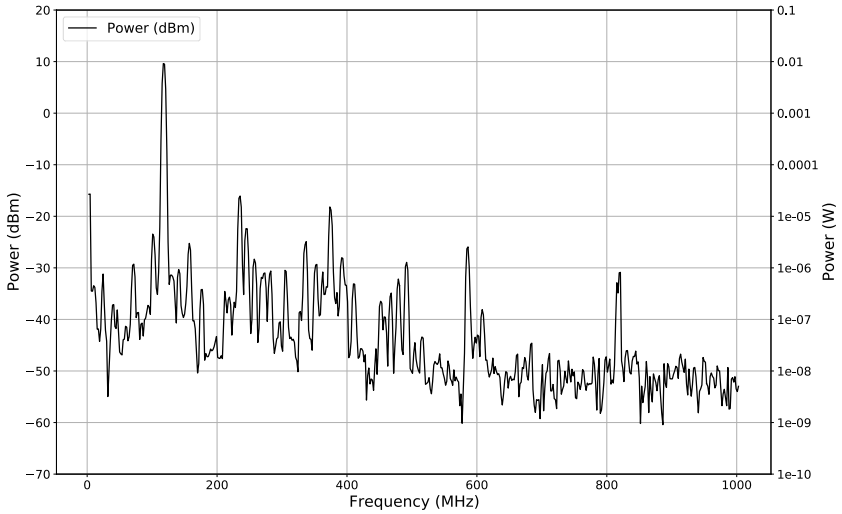

Figure 3.6.: Master and imaging laser beat signal mixed with a VCO signal and filtered with a low pass. The dominant mode is used for further processing and split and superimposed with itself after a delay line. The higher orders are suppressed as much as possible.

The signal is then divided into two parts, one of which travels through the delay line for a longer time and is recombined by mixer 2 which acts as a phase detector. Afterwards, the unwanted frequencies are again filtered with a second low pass filter.

The finalized lockbox with all soldered components is displayed in Figure 3.7. All components are powered by a STATRON power supply (model 6371.16) which is connected through a D-Sub 9 connector on the back of the lockbox. Which pin on the connector carries which voltage and is connected to which part in the box is given in Table 3.4.

Table 3.4.: Power supplied to some of the Lockbox components from a STATRON power supply through a D-Sub 9 connector

Pin Nr.	color flat ribbon cable	Voltage[V]	supplied component
1	gray	−15	-
2	blue	−12	-
3	yellow	−5	-
4	red	0	VCO (GND)
5	black	5	VCO
6	lilac	12	Amplifier 1, Amplifier 2
7	green	15	Amplifier 3
8	orange	0	Amplifier 3 (GND)
9	brown	0	Amplifier 1 (GND), Amplifier 2 (GND)

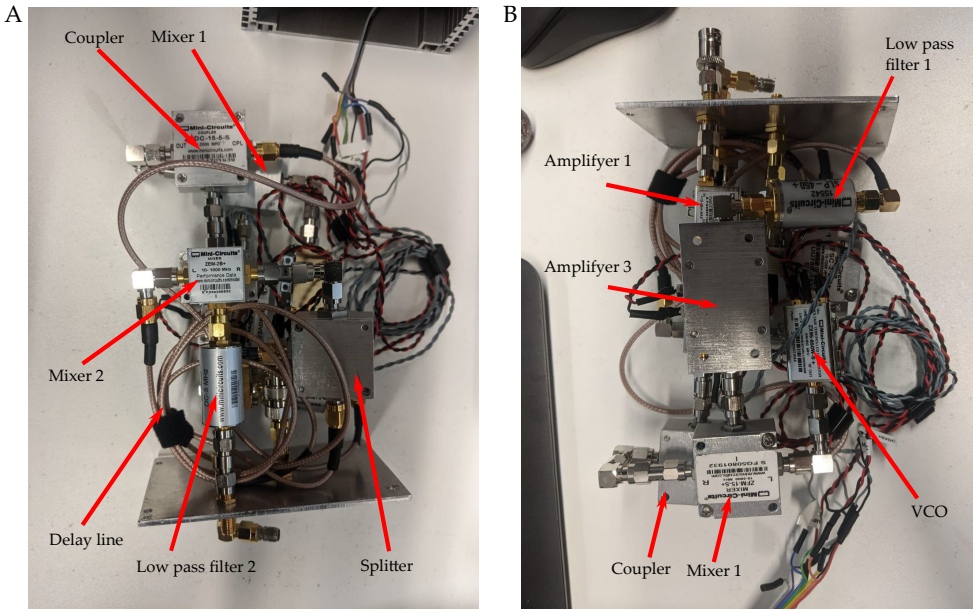

Figure 3.7.: **A, B)** pictures of the finalized lockbox setup. Since the box holding the components is relatively small, fitting the setup into it was only possible using this specific configuration.

3.2.3. Error Signal and Lock

The output of the lockbox is used as an error signal to lock the high field imaging laser on (see Figure 3.8). Using this error signal and a PID, the feedback loop for locking the laser was implemented. With the VCO voltage V_{tune} the offset lock frequency can be tuned even while the laser is locked, given V_{tune} is changed slowly enough. The error

signal has a large enough amplitude and slope to produce a stable lock. The single biggest reason why the laser would fall out of lock was either the master laser or the imaging laser multimoding.

In order to see a proper error signal, both master laser and imaging laser must be in single mode operation. The absence of the resonance peak in one of the error signal valleys can be a good indicator, that one of the lasers is multimoding. The shape of the error signal changes during multimode operation of either of the lasers. The error signal for this case is plotted in Figure 3.9. How to deal with multimoding lasers is described in Section Troubleshooting.

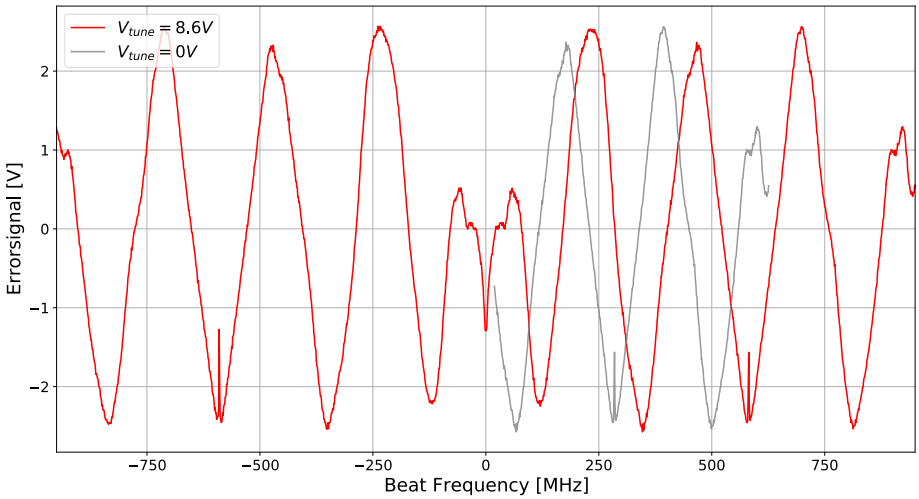

Figure 3.8.: High field imaging error signal against beat frequency for a VCO tuning voltage of $8.6V$ (indicated in red). For smaller tuning voltages the signal becomes slightly steeper and shifts. This is indicated with an example error signal for $V_{\mathrm{tune}} = 0V$. Using this, the zero crossings of the error signal can be shifted to different offset frequencies and therefore the offset set point adjusted.

With the monitor output of the lockbox the beating frequency of the lasers can be checked while locking the laser with either a frequency counter or a spectrum analyzer if it has to be more accurate. A small jitter of the frequency of around 3 MHz was observed while the lasers were locked. Whether this is an issue for the imaging has to be determined in the future.

3.3. Troubleshooting

If the high field imaging laser falls out of lock it is likely for some of the following reasons. Most of them are easily checked and fairly quickly fixed.

Master Laser Out Of Lock

If the master laser is out of lock, the imaging laser will follow and ultimately fall out of lock as well. The imaging laser error signal is usually only visible when the master laser is locked. Always make sure the reference is locked and in single mode operation before proceeding with the imaging setup.

Wrong Frequencies

If the frequencies of the two lasers are too far apart, there will be no error signal. If the master laser is locked on the correct spectroscopy signal, only the imaging laser has to be adjusted. As a first approach, one can check whether the error signal can be found by tuning through the piezo voltage. If this quick fix does not work, one can use the fiber coupled wavemeter by blocking the beam coming from the master laser and plugging out the fiber from the photo diode. Rather than setting the frequency to the literature value, it is oftentimes more useful to set it to the value the wavemeter shows for the locked master laser. This avoids calibration issues with the wavemeter.

If one has trouble locking the master laser, the same fiber can be used to set the frequency close to the literature value and hopefully find the spectroscopy signal. Here it is important to make sure that the wavemeter displays the vacuum value of the wavelength and not the significantly smaller air value. Otherwise, the wavemeter value cannot be compared to the literature value for the D_2 transition (766.701 nm) which is commonly given as a vacuum value.

Setup Misaligned

One can tell that the setup is misaligned by checking whether there is enough signal on the photo diode. The photo diode output can be quickly checked with an oscilloscope. Blocking the beams should significantly lower the signal. If the signal stays the same after blocking a beam, the setup is misaligned.

The recoupling should be done by plugging out the fiber and using an outcoupler

with a powermeter. Chances are that there is still some signal in the fiber, which could be lost by trying to optimize with the oscilloscope. If both beams are misaligned, always start with the master laser beam. It is aligned with the 50:50 beam splitter and the mirror before the fiber (Figure 3.3) which futher misaligns the imaging laser beam. Afterwards, the imaging laser beam can be aligned using the PBS and the mirror before the 50:50 beam splitter. If only the master laser beam is misaligned, the imaging laser beam has to be readjusted afterwards for the same reason.

Multimoding Lasers

This is by far the most common reason the lasers fell out of lock. Especially the imaging laser is prone to multimoding. It falls out of lock multiple times a day on days with large humidity changes. During winter, it would fall out of lock every night. This became somewhat more stable in the summer. If this does not change with more stable conditions in the lab, I would recommend considering exchanging the laser or the diode.

There are a few ways one can tell whether the lasers are multimoding. The most straightforward one is checking the Fabry-Perot interferometer. By blocking one beam and checking the signal on the Fabry-Perot oscilloscope, one can quickly find out which laser is multimoding. Only one intense peak should be visible. As shown in Figure 3.9, one can also tell by the shape of the error signal, that one or both of the lasers are multimoding. When looking at the beat signal with a spectrum analyzer, the beat appears as a broad hill instead of a large well-defined peak when multimoding. The spectroscopy lock railing while the imaging laser is still locked can also be an indicator.

Sometimes the behavior can be fixed by adjusting the piezo voltage of the laser, but oftentimes, touching other parameters is required. A combination of adjusting the diode current, piezo voltage, and set temperature proved successful most of the time. I often found it helpful to turn off feed forward during this process. After touching the diode temperature, one should check again after some hours whether the new setpoint is truly more stable. When adjusting so many of the parameters it was usually helpful to use the wavemeter simultaneously to make sure one does not jump away from the desired frequency. Ideally, one should try to keep an eye on the Fabry-Perot interferometer, wavemeter, and spectroscopy/error signal instead of just focusing on one of them.

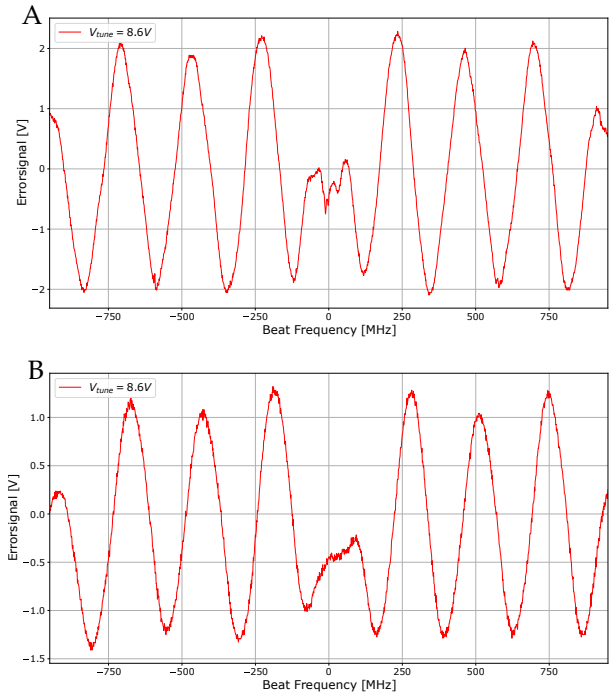

Figure 3.9.: High field imaging error signal against beat frequency for $V_{\text{tune}} = 8.6V$
A) where the imaging laser is multimoding.
B) where both lasers are multimoding.
when compared to Figure 3.8, the signal becomes more noisy, less defined and most notably the characteristic peak in one of the valleys is missing.

Other Sanity Checks

Lastly, the following things need to be in place for the lock to work. Though they usually do not break by themselves but rather could be changed by someone who forgot to put them back, it is worth checking them if nothing else works.

1. **VCO Not Grounded.** If the VCO is not grounded, the floating ground usually does not kick the laser out of lock but does influence the offset frequency. It slowly wanders up and down despite the lock.

2. **Lockbox Not Powered.** Make sure the lockbox is connected to a power supply via the D-Sub 9 connector on the back. The screws on the side have to be screwed in to ensure there is no loose contact. When connecting the spectrum analyzer to the monitor output of the lockbox, one can see it jump from no signal to signal when plugging in the lockbox.

3. **Bad PID Parameters.** If the lock is unstable for reasons other than the ones mentioned above, it might be worth revisiting the PID parameters.

CHAPTER 4

Sodium: D_1 grey molasses

The grey molasses setup can be divided into three parts: the spectroscopy setup for locking the laser, the grey molasses setup for producing the needed frequencies, and the experimental table setup for shining the grey molasses light onto the atoms. The first two parts of the setup were subject of my thesis and will be described in Sections Spectroscopy setup and Grey molasses setup. The setup on the experimental table is simply the unaltered MOT setup, which is described in [30]. The following section introduces the theoretical concepts needed to understand the grey molasses setup.

4.1. Theory and Motivation

4.1.1. Motivation

Though it is possible to achieve Bose-Einstein Condensation (BEC) without a grey molasses it is, in our case, preferable to include a grey molasses for sodium. Previously, sodium was cooled with a dark-SPOT magneto-optical trap (MOT), a microwave evaporation in a magnetic trap, and finally evaporative cooling in a crossed optical dipole trap (cODT). With this, a sodium BEC was achieved [30].

When adding potassium, it becomes more tedious to condense. Loading both species into a dual-species MOT already led to increased losses especially of potassium, probably due to light-assisted collisions. Then, in dual-species operation, a grey molasses for potassium and an optical molasses for sodium was employed to further cool down the sample before loading into the magnetic trap. The microwave evaporation with two species present proved to lead to major losses of either one or the other species. While a steeper trap could mitigate this behavior, it also led to significant heating. With this sequence, condensation of the two species could not be achieved [30].

With the help of the grey molasses I implemented, it was indeed possible to conserve more atoms while reaching similar temperatures at the end of the grey molasses compared to the end of the microwave evaporation in single-species operation. Following

the dual-species MOT with a grey molasses for each species alleviated the need for a microwave evaporation. Given the temperatures are low enough after the grey molasses, the cloud could be compressed with a magnetic trap and loaded directly into the dipole trap, avoiding the losses during the microwave evaporation. With this, a single-species sodium BEC could be produced without the help of the microwave evaporation (see Section 4.3.2). The new sequence still remains to be optimized for dual-species operation.

In the following Section, I will focus on the working principle of a grey molasses. For a comprehensive introduction to several other cooling techniques like the previously mentioned magneto-optical traps, optical molasses, and dipole traps one can consult [18]. The microwave evaporation in the magnetic trap which the grey molasses setup aims to replace is presented and explained in Jan Kilinc's doctoral thesis [30].

4.1.2. Working principle

Doppler cooling methods like magneto-optical traps (MOTs) are commonly used to cool atom clouds which are coming from an oven. They are useful for reducing the temperature of a sample substantially. However, they cannot increase phase space density sufficiently to achieve Bose-Einstein condensation. This is due to the fact that through Doppler cooling one can only reach a finite temperature

$$T_D = \frac{\hbar\gamma}{2k_B} \tag{4.1}$$

which depends on the line width γ of the excited state [18].

There exist, however, methods to go below this Doppler limit. This is possible when more than two energy levels are included in the process. The first sub-Doppler temperatures were achieved with Sisyphus cooling [51], which was first explained by Jean Dalibard and Claude Cohen-Tannoudji [52]. Since Sisyphus cooling, similarly to grey molasses cooling, utilizes polarization gradients, it is instructional to understand Sisyphus cooling first.

When two counter-propagating laser plane waves with the same frequency ω_L and electric field strengths $\mathcal{E}_0$ and $\mathcal{E'}_0$ are overlapped, the total electric field $\mathbf{E}(z,t)$ be-

comes

$$\mathbf{E}(z,t) = \mathcal{E}^+(z)\exp(-i\omega_L t) + c.c. \tag{4.2}$$

$$\text{where } \mathcal{E}^+(z) = \mathcal{E}_0\epsilon e^{ikz} + \mathcal{E'}_0\epsilon' e^{-ikz}. \tag{4.3}$$

In the case that the polarizations ϵ and ϵ' are opposite circular polarizations, the positive frequency component $\mathcal{E}^+(z)$ becomes

$$\mathcal{E}^+(z) = \frac{1}{\sqrt{2}}(\mathcal{E'}_0 - \mathcal{E}_0)\epsilon_X - \frac{i}{\sqrt{2}}(\mathcal{E'}_0 + \mathcal{E}_0)\epsilon_Y \tag{4.4}$$

$$\text{with } \epsilon_X = \epsilon_x\cos(kz) - \epsilon_y\sin(kz) \tag{4.5}$$

$$\text{and } \epsilon_Y = \epsilon_x\sin(kz) - \epsilon_y\cos(kz). \tag{4.6}$$

Therefore, the total electric field is the superposition of two fields with amplitudes $(\mathcal{E'}_0 - \mathcal{E}_0)/\sqrt{2}$ and $(\mathcal{E'}_0 + \mathcal{E}_0)/\sqrt{2}$. From equations (4.2) to (4.6) one can deduce that the polarization of the total electric field rotates when moving along z, but keeps the same ellipticity. This means that there is no polarization gradient but only a rotation of the same polarization. The periodicity of the rotation occurs with the wavelength $\lambda = 2\pi/k$ [52].

In the case that the polarizations of the two beams are orthogonal and linear with

$$\epsilon = \epsilon_x \tag{4.7}$$

$$\text{and } \epsilon' = \epsilon_y, \tag{4.8}$$

the positive frequency component becomes

$$\mathcal{E}^+(z) = \mathcal{E}_0\sqrt{2}\left(\cos\left(kz\frac{\epsilon_x+\epsilon_y}{\sqrt{2}}\right) - i\ \sin\left(kz\frac{\epsilon_y-\epsilon_x}{\sqrt{2}}\right)\right) \tag{4.9}$$

where for simplicity it was assumed that the lasers have the same amplitude $\mathcal{E}_0$. Here the ellipticity changes when one moves along z. For $z = 0$, the resulting polarization ϵ_{tot} is linear along $\epsilon_1 = (\epsilon_x+\epsilon_y)/\sqrt{2}$, for $z = \lambda/8$ it is circular (σ^-), for $z = \lambda/4$ linear along $\epsilon_2 = (\epsilon_x - \epsilon_y)/\sqrt{2}$, for $z = 3\lambda/8$ circular again (σ^+), and so on [52].

This polarization gradient in space is necessary for the Sisyphus and grey molasses scheme to work. In Sisyphus cooling, the polarization gradient acts on three bare states. Consider, for example, an atom in such a light field which drives a transition

with $J_g = 1/2 \longleftrightarrow J_e = 3/2$. If there is no gradient, the two Zeeman sublevels $g_{1/2}$ and $g_{-1/2}$ of the ground state do not experience a relative energy shift and no variation in energy shift depending on z. However, if there is a polarization gradient, the energies of the ground states start oscillating periodically due to the periodically varying polarization. The Zeeman sublevels do not oscillate synchronously but oppositely. For a more detailed discussion on why this is the case, one can consult [52]. In Figure 4.1, the discussed energy and polarization changes are illustrated.

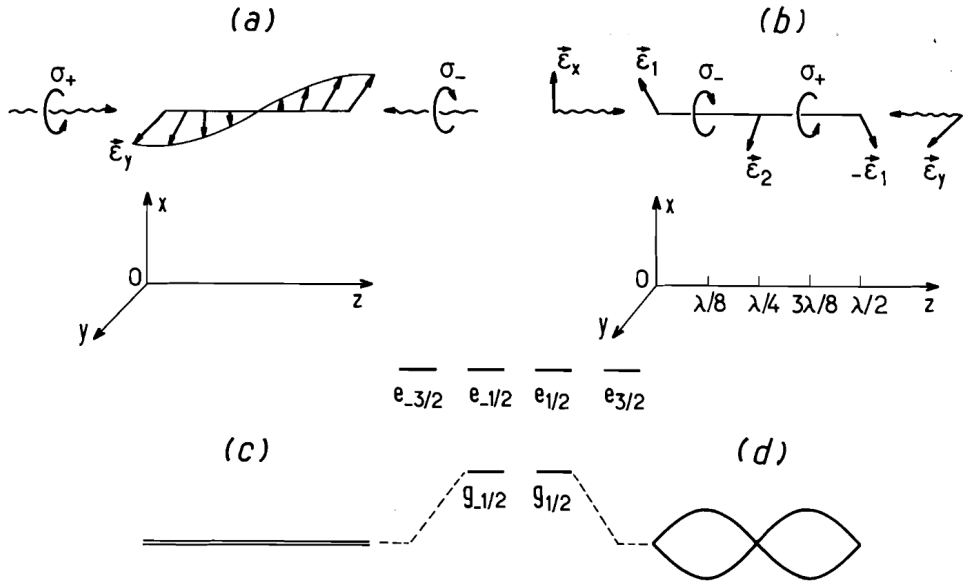

Figure 4.1.: **A)** Resulting polarization rotation in space for two counter-propagating circularly polarized beams.
B) Resulting polarization for two counter-propagating orthogonally linearly polarized beams. The resulting ellipticity varies in space.
C) The light shift energies for a σ^+-σ^- configuration do not vary in space.
D) For a lin $\perp$ lin configuration, the light-shifted energies oscillate with a period $\lambda/2$. The different Zeeman sublevels experience relative shifts. The figure was taken from [52].

For Sisyphus cooling, one can now utilize that the $J_g = 1/2 \longleftrightarrow J_e = 3/2$ can only be driven by circularly polarized light due to selection rules. The atoms must first climb the potential hill to a maximum while losing kinetic energy. At these maxima, they have the highest probability of being excited. After traveling a distance $\lambda/4$, they are de-excited by oppositely circular polarized light. They fall back into a state which is minimal at this position and need to climb another potential hill. This process can be repeated until the recoil limit $T_{\text{recoil}} = \frac{(h/\lambda)^2}{2mk_B}$ is reached. This recoil limit is a consequence of the discrete velocity changes that result from the absorption processes. It

can be surpassed with evaporative cooling [18].

The difference between grey molasses cooling and Sisyphus cooling lies, among other things, in the involved energy levels. In grey molasses cooling, the polarization gradient acts on three dressed states. For the most simple possible configuration, consider a three-level scheme in Λ configuration where the two ground states $|1\rangle$ and $|2\rangle$ are coupled through a field with an excited state $|3\rangle$. The field's frequency is blue detuned by δ (see Figure 4.2). In the case that the two ground states have an equal energy, the Hamiltonian for the system becomes

$$\mathbf{H} = \mathbf{H_0} + \mathbf{V} \tag{4.10}$$

$$= \frac{\hbar}{2}\begin{pmatrix} 0 & 0 & 0 \\ 0 & 0 & 0 \\ 0 & 0 & -2\delta \end{pmatrix} + \frac{\hbar}{2}\begin{pmatrix} 0 & 0 & \Omega_1 \\ 0 & 0 & \Omega_2 \\ \Omega_1 & \Omega_2 & 0 \end{pmatrix}. \tag{4.11}$$

Here Ω_1 and Ω_2 are the Rabi frequencies of state $|1\rangle$ and $|2\rangle$ respectively [53].
The eigenvalues and eigenstates of this Hamiltonian are given by

$$\lambda_D = 0 \tag{4.12}$$

$$\lambda_{B_1} = -\delta - \sqrt{\Omega_1^2 + \Omega_2^2 + \delta^2} \tag{4.13}$$

$$\lambda_{B_2} = -\delta + \sqrt{\Omega_1^2 + \Omega_2^2 + \delta^2} \tag{4.14}$$

$$|\Psi_D\rangle = -\frac{\Omega_1}{\Omega_2}|1\rangle + |2\rangle \tag{4.15}$$

$$|\Psi_{B_1}\rangle = \frac{\Omega_1}{\lambda_{B_1}}|1\rangle + \frac{\Omega_2}{\lambda_{B_1}}|1\rangle + |3\rangle \tag{4.16}$$

$$|\Psi_{B_2}\rangle = \frac{\Omega_1}{\lambda_{B_2}}|1\rangle + \frac{\Omega_2}{\lambda_{B_2}}|1\rangle + |3\rangle. \tag{4.17}$$

Here only the bright states $|\Psi_{B_1}\rangle$ and $|\Psi_{B_2}\rangle$ couple with $|3\rangle$. The dark state $|\Psi_D\rangle$ has no overlap with state $|3\rangle$ and therefore atoms in this state cannot be excited to state $|3\rangle$ with the blue detuned light [53].

Due to the fact that only the bright states interact with the light field, only these states experience a spatially modulated light shift in the case that there is a polarization gradient. The potential of the dark state stays constant in space. The dependence of the bright states on the polarization lies within the Rabi frequencies $\Omega_i = \langle i| e\mathbf{z} \cdot \boldsymbol{\epsilon}\mathcal{E}_0 |3\rangle /\hbar,\ i = \{1, 2\}$ [54]. When two counter-propagating blue de-

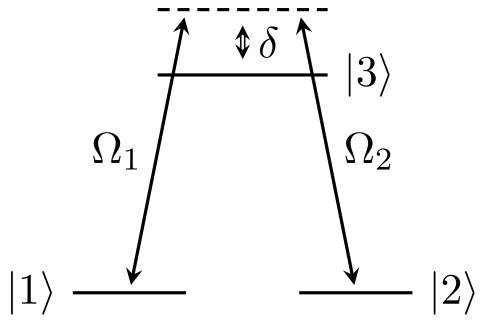

Figure 4.2.: Three level Λ scheme. A laser blue-detuned by δ couples ground states $|1\rangle$ and $|2\rangle$ with excited state $|3\rangle$ with Rabi frequencies Ω_1 and Ω_2 [53].

tuned beams with orthogonal linear polarization are overlapped they therefore create a sinusoidal potential for the bright state similar to the potentials used for Sisyphus cooling [30]. This potential landscape is shown in Figure 4.3.

Similar to Sisyphus cooling, the atoms lose their kinetic energy by climbing the potential hills in the bright states. The transition to the excited state is most probable at the top of the potential hill. Even though the dark state is not coupled to the excited state via the light field, it is allowed via selection rules and therefore possible for the excited state to decay into the dark state by spontaneous emission. The only way atoms can leave the dark state is through motional coupling. The probability $P \propto \langle \Psi_{B_i} | \frac{\mathbf{p}^2}{2M} | \Psi_D \rangle \propto v$ is proportional to the velocity v of the atom. This means that the faster the atoms are, the likelier it is that they are excited into the bright state and undergo another cycle. The colder atoms remain in the dark state. Because the transition from dark state to bright state is likeliest at the valley where the states have the smallest energy difference, the atoms oftentimes have to climb another potential hill before being excited and de-excited again. On average, they therefore lose energy with each cycle which is carried away by the emitted photon. The system's temperature is thus reduced without a loss of atoms, which helps increase the phase space density. This is called velocity-selective coherent population trapping (VSCPT) [55] [30].

In the grey molasses scheme I implemented, some of the assumptions made in this introduction are not strictly fulfilled. The D_1 transition of ^{23}Na, which is used for the implementation of the grey molasses is not truly a Λ scheme (see Figure 4.9). In reality, there are more hyperfine levels close to the levels desired for the scheme which will also mix into the eigenstates of the system. This means that there is no dark state but rather a "grey state" which ever so slightly still couples with the excited state. It is for

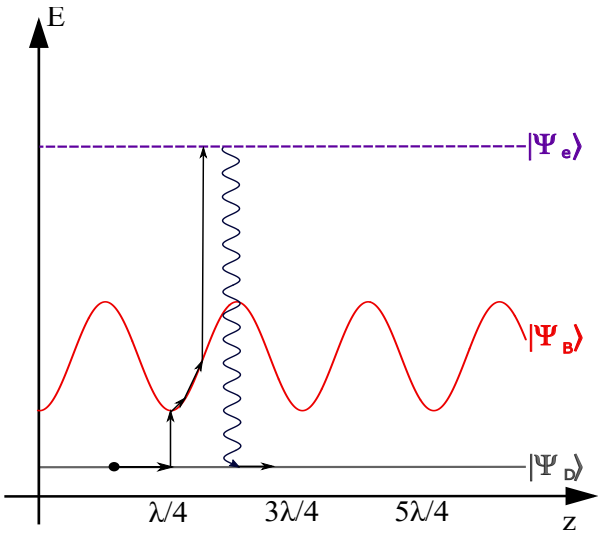

Figure 4.3.: Working principle of grey molasses cooling. A polarization gradient sinusoidally modulates the energy of the bright state $|\Psi_B\rangle$ while the energy of the dark state $|\Psi_D\rangle$ is constant. Atoms are most likely coupled from the dark state to the bright state in the valley of the bright state potential and if they are fast. From there, they climb the potential hill, losing kinetic energy. At the top of the potential hill, they are most likely to be excited to $|\Psi_e\rangle$ from where they can decay back into the dark state. Atoms go through multiple cycles until they have lost so much kinetic energy that they do not couple to the bright state and remain in the dark state. Figure adapted from [55].

this reason, that the cooling technique is called grey molasses.

More so, the assumption that both ground states have the same energy is not true for our scheme. This leads to an additional perturbation term on the diagonal of $\mathbf{H}_0$ in Equation (4.11). It alters the eigenvalues of the bright states but does not change the working principle of the grey molasses.

Finally, the assumption that polarizations of the overlapping beams are linear is not true for our setup. So long as the beams are elliptical but not circular, they will still produce a polarization gradient, albeit a smaller one the more elliptical the beams are. The grey molasses cools less efficiently but still works in this case.

4.2. Setup

4.2.1. New Fiber Laser Setup

To be able to implement a grey molasses using the D_1 line of ^{23}Na, some alterations to the existing laser table setup for sodium had to be made. The 2D and 3D MOT of sodium are operated with D_2 light. Due to the fact that the D_2 transition (589.158 nm) and the D_1 transition (589.756 nm) [54] have too different frequencies to be able to both produce lights by shifting the frequency of one laser, a different laser for the grey molasses had to be introduced.

Originally, most of the D_2 light, including the 2D-MOT, 3D-MOT, imaging, push and repumper light was provided by a Toptica TA-SHG-pro. Since the SHG could not provide enough power for all of the needed beams, a second Toptica SHG produced the slower beam with an offset lock [30]. For the new setup, the two SHGs were switched out with a more powerful fiber laser (MPBC VRFA-SF-Series, pumped by MPBC YFL-P Series). It provides enough power for all MOT and imaging beams, including the slower beam. The old setup was left mostly intact. The SHG was switched out with the fiber laser and a 1:2 telescope for matching the SHG waist. A double pass for producing the slower beam was added to the D_2 setup. The new D_2 setup, including all the alterations is shown in Figure 4.4. In Table 4.1, typical laser powers for the D_2 beams before and after the fiber that leads to the experimental table are listed.

This process of switching out the laser freed up two SHGs which were then both available for the D_1 grey molasses. Both SHGs were placed on a breadboard mounted 25 cm above the laser table. The former master laser which provides 1.4 W of power is now used for D_1 light for the grey molasses. The second (former follower) SHG was kept as a spare.

Table 4.1.: Typical powers for D_2 beams before and after coupling.

Laser beam	power before fiber [mW]	power after fiber [mW]
2D-MOT	384	183
Coarse Imaging	0.13	0.06
Fine Imaging	1.85	0.3
Push	23	4.1
Slower	900	235
Dark Spot Repumper	21.4	11.2
3D-MOT Repumper	50	26.7
3D-MOT	53	25

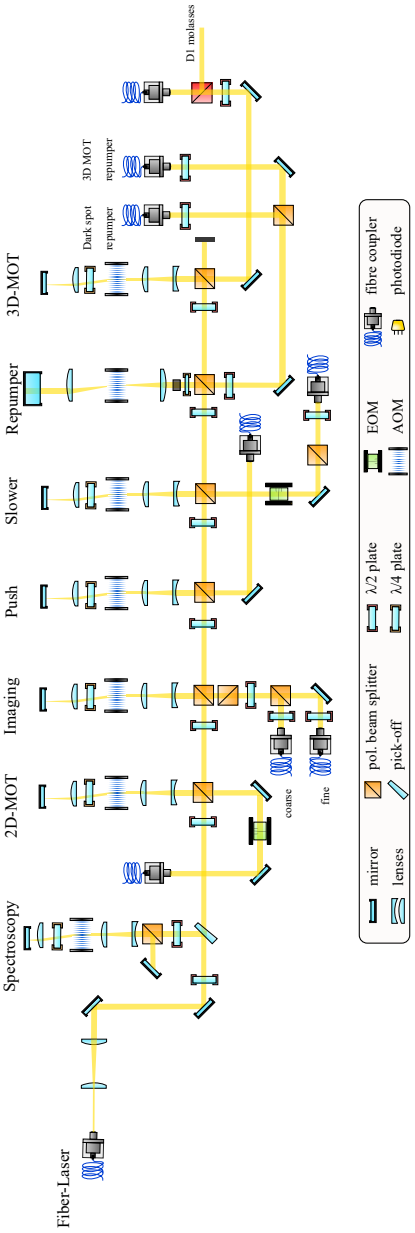

Figure 4.4.: New laser table setup sodium D_2 light. Most notably the SHG was switched out with a more powerful fiber laser and a telescope for matching the spacial mode to the existing setup. A double pass for producing the slower beam for the 2D-MOT was added between the push and repumper paths. Compared to before, the couplers were rearranged a little bit. Finally, a 50:50 beam splitter was added before the 3D-MOT fiber. This allows for coupling the D_1 molasses light into the same fiber. Adapted and altered from Figure 3.5 in [30].

4.2.2. Spectroscopy Setup

Shortly before and during the process of switching the lasers, the old spectroscopy cell which was originally used for locking the SHGs broke down slowly over the course of several days. The amplitude of the photo diode and error signal slowly shrunk, worsening the signal-to-noise ratio and the stability of the lock. Heating the spectroscopy cell to higher temperatures could improve the signal in the short term, but in the long term seemed to accelerate the breakdown of the cell. On the surfaces of the cell, especially in the places that were heated the least, a brown residue could be found. Sodium in its pure form should appear in a grey, silver, metallic color. We therefore suspect that a chemical reaction that was accelerated at higher temperatures bound the sodium to the cell and subsequently reduced the vapor pressure in the cell over time. For this reason, a new cell was prepared which indeed did not deteriorate like the old cell.

The breakdown of the old spectroscopy cell was not the only reason a new setup for the cell was needed. In the new setup, two lasers need to be locked to two different transitions: a fiber laser needs to be locked to the D_2 ($^2S_{1/2} \leftrightarrow {}^2P_{3/2}$) transition of sodium and a Toptica SHG needs to be locked to the D_1 ($^2S_{1/2} \leftrightarrow {}^2P_{1/2}$) transition of sodium. Furthermore, the space that was previously used for the spectroscopy setup was freed up for the fiber laser. The new spectroscopy setup was constructed on the breadboard that was introduced to hold the SHG units.

For the new spectroscopy setup, we opted for a Saturated Absorption Spectroscopy (SAS) scheme similar to the setup for potassium which is described in [30]. In SAS, two counterpropagating laser beams pass through a cell that contains a vapor of the atoms that one wants to use as a reference for a lock. In our setup, the counterpropagating beams are produced by reflecting the same beam back onto itself. When the beam first passes the sample, it excites a portion of atoms that depends on the frequency of the light. Directly on resonance, the most atoms are excited and the absorption of the beam is highest. Close to the resonance, there is still a finite probability for the atoms to be excited by the beam. This probability depends on the natural linewidth and, because of Doppler broadening, on the temperature of the atoms. Unfortunately, in our case, the Doppler broadening is larger than the separation of the hyperfine states. This means that with one beam alone, the resolution of the spectroscopy would not suffice for locking to a transition between specific hyperfine states [56].

The second beam makes it possible to resolve transitions that fall within the same

Doppler valley. After the first pump beam has excited the atoms, the second probe beam falls onto the atoms, which were excited by the first beam. In the case that the beams are detuned from a resonance, they will excite atoms in different velocity classes. Here the absorption of the probe beam is not affected. In the case that both beams are on a resonance, the pump beam has already saturated the sample. For the weaker probe beam absorption becomes much less likely. When varying the frequency of the beams in this setup, one observes the Doppler valley with reduced transmission and within this Doppler valley, small Lamb dips with increased transmission compared to the valley. At the frequency of these absorption dips both beams excited the same atoms with velocity $v = 0$ in the direction of the beam. The frequency where the dip occurs is therefore not Doppler shifted. [56]

In the case that several hyperfine transitions fall into the same Doppler valley, more features than the Lamb dips corresponding to the transitions appear. At the arithmetic mean between two Lamb dips, a crossover resonance in the form of a dip or peak appears. If the two states share a ground state (V-System), the crossover resonance is a peak in the transmitted intensity. If the states share an excited state (Λ-System), a dip appears. For further reading on Saturated Absorption Spectroscopy, [57], [58], and [56] can be consulted. Especially Chapter 8.3 in [56] provides a concise description and explanation of the working principle of SAS and the appearance of crossover resonances.

For our new spectroscopy setup both Saturation Absorption Spectroscopies for the D_1 and the D_2 laser share the same spectroscopy cell. For this, a Thorlabs GC25075-NA glass cell filled with sodium was wrapped in a copper wire (see Figure 4.5 A). The copper wire acts as a coil producing a small magnetic field when a changing electrical current is applied. This is used for locking via frequency modulation spectroscopy (FMS) and explained more thoroughly at the end of this section.

At room temperature, the vapor pressure of sodium is too low for a successful operation of the spectroscopy. Therefore, the spectroscopy cell is placed in custom-made brass cylinders which conduct and distribute the heat of two mineral-insulated band heaters. Two small holes on the ends of the cylinders allow for light to pass through the cell. An unheated area is left open between the two brass cylinders such that the sodium condenses in the middle of the cell, rather than the windows of the cell in case it is cooled down (see Figure 4.5 B). The temperature is stabilized using a K-type thermocouple which is fixed on the coils below the brass. Its signal is amplified with

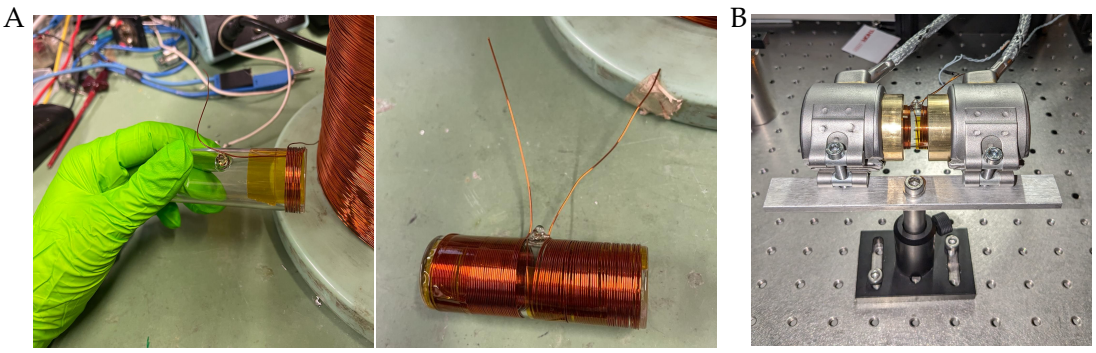

Figure 4.5.: Sodium spectroscopy cell setup.
A) The cell is tightly wrapped in one layer of copper wire which is secured with Kapton tape.
B) In the finalized spectroscopy cell setup, two brass cylinders distribute the heat of two band heaters.

a MAX31855 breakout board and received by an Arduino Uno which acts as a PID. A phase angle dimer (NS 80) controlled by the Arduino Uno provides the current for the heaters. A first faint spectroscopy signal could be observed starting at temperatures of 100 °C. The current set point of the temperature is chosen at 160 °C.

The optics setup surrounding the spectroscopy cell is displayed in Figure 4.6. It was constructed on the breadboard mounted 25 cm above the laser table, next to the SHG providing the D_1 light. With a beam sampler, roughly 30 mW of power are picked off for the D_1 spectroscopy. A telescope reduces the waist of the D_1 beam to minimize the overlap between the two beams in the cell which helps avoid coupling the two spectroscopy signals to each other. With a $\lambda/2$-plate and a polarizing beam splitter, the power going into the spectroscopy cell can be further reduced to avoid power broadening the signal too much. The optimal signal was found at 11 mW of D_1 light. A $\lambda/4$-plate circularly polarizes the light which is necessary for driving the transitions. After passing the spectroscopy cell once, the beam is reflected onto itself with a D-mirror, which leaves space for the second D_2 beam to also enter the cell. The D_1 beam passes the cell and $\lambda/4$-plate a second time and is reflected onto a photo diode. The D_2 light coming from the fiber laser uses similar components to pass through the cell twice.

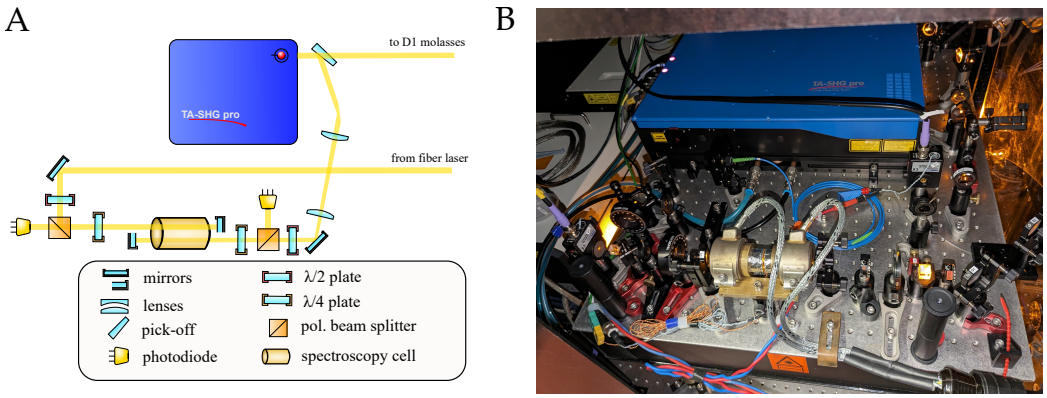

Figure 4.6.: Sodium spectroscopy optics setup.
A) Schematics of the optics setup. The D_1 and D_2 lasers share one spectroscopy cell.
B) Picture of the sodium spectroscopy setup.

From the photo diode signals, error signals for locking the lasers are produced via Frequency Modulation Spectroscopy (FMS) for both the fiber laser and SHG. There are generally two different ways to approach FMS. One possibility is to periodically modulate the frequency of the laser at a low repetition rate and low amplitude. If the laser is close to an atomic resonance where a dip or valley appears on the photo diode signal, the frequency modulation (FM) should translate to a significant amplitude modulation (AM). The ratio of AM to FM for each frequency then yields the derivative of the spectroscopy signal which is used as an error signal [59] [60].

Rather than varying the frequency of the laser, one can also modulate the absorption frequencies by using the Zeeman effect and shifting them with an outer magnetic field. This is then called Zeeman modulation locking [61]. In our setup, the magnetic field within the cell is varied by applying a small sinusoidally varying current ($f \approx 80\,\mathrm{kHz}$) to the copper coil that was wrapped around the cell. The error signal is then produced by using the varying current (FM) as a reference signal for a lock-in amplifier and the photo diode signal (AM) as the main input. This error signal has zero crossings at the center of Lamb dips or crossover resonances and a linear relationship between amplitude and detuning in regions close to the zero crossings. With a PID, the lasers can then be locked to any of the Lamb dips or crossover resonances. The D_1 and D_2 photo diode and error signals are displayed in Figures 4.7 and 4.8 respectively.

For both D_1 and D_2 signals, several hyperfine transitions and crossover peaks are visible within the same Doppler valley. For the D_1 signal, all possible transitions between the hyperfine manifolds of the ground and excited states and their crossover peaks can be resolved. In the D_2 spectroscopy signal, the peaks for different ground state manifolds can be resolved, but the excited state peaks overlap and form one peak due to power broadening. With this signal, the fiber laser was locked to the $|F = 2\rangle \rightarrow$ excited-transition of the D_2 line which is used for 2D-MOT, 3D-MOT and imaging. The SHG on the other hand was locked to the $|F = 2\rangle \rightarrow |F' = 1\rangle$-transition of the D_1 line. In the following Section (Grey molasses setup), the choice of the lockpoint and the subsequent shifting of this frequency for the grey molasses is explained.

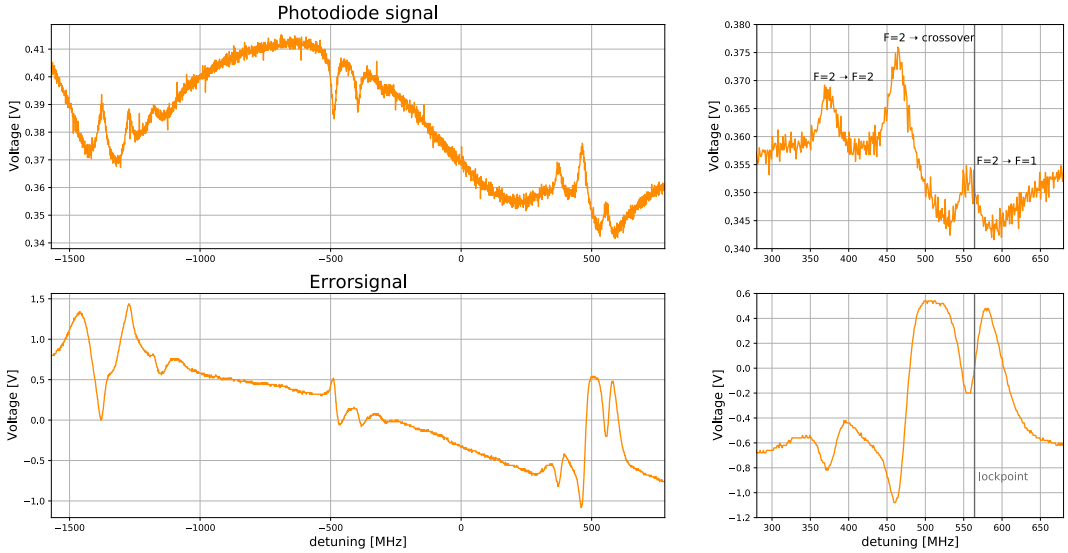

Figure 4.7.: Sodium D_1 spectroscopy signal and error signal. The detunings are given relative to the fine structure prediction for the D_1 transition. The SHG is locked to the $|F = 2\rangle \rightarrow |F' = 1\rangle$-transition with this signal. The lock point is indicated with a grey line.

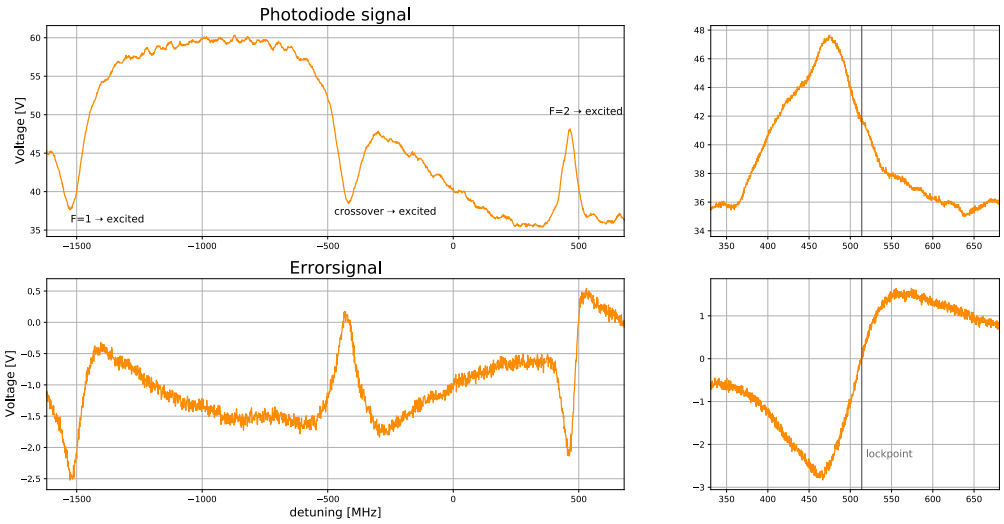

Figure 4.8.: Sodium D_2 spectroscopy signal and error signal. The detunings are given relative to the fine structure prediction for the D_2 transition. Only the ground state manifolds but not the excited state hyperfine manifolds can be resolved. The fiber is locked to the $|F = 2\rangle \rightarrow$ excited-transition with this signal. The lockpoint is indicated with a grey line.

4.2.3. Grey Molasses Setup

In the previous section, the implementation of the SHG-lock to the $|F = 2\rangle \rightarrow |F' = 1\rangle$-transition of the of the sodium D_1 line was presented. As explained in Section 4.1.2, one frequency is not sufficient for implementing a grey molasses scheme since at least three energy levels need to be coupled to each other to produce a dark or grey state. Ideally, one would want to use a three-level Λ-scheme for the grey molasses and avoid mixing with any other states. We therefore chose to implement the grey molasses using the $|F = 1\rangle$ and $|F' = 2\rangle$ manifolds of the ground state and the $|F' = 2\rangle$ manifold of the excited state (see Figure 4.9). The blue detuning needed for the grey molasses helps to avoid mixing the undesired $|F' = 1\rangle$ manifold of the excited state too much.

Even though the second frequency in the grey molasses scheme serves a different purpose than the repumper in a Doppler cooling method, the two frequencies are still commonly referred to as "cooler" and "repumper". In the case of the grey molasses "repumper" is used to refer to the mode with lower laser power. While this convention will be followed in this thesis, it is helpful to remember, that in the grey molasses scheme, the mode with lower intensity is not an optional addition to close a cooling cy-

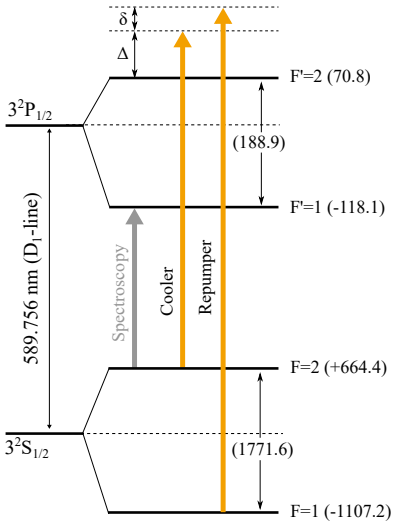

Figure 4.9.: Energy level scheme for ^{23}Na. The $|F = 2\rangle \rightarrow |F' = 2\rangle$ and $|F = 1\rangle \rightarrow |F' = 2\rangle$ transitions of the D_1 line are used as cooler and repumper of the grey molasses respectively. The spectroscopy is locked to the $|F = 2\rangle \rightarrow |F' = 1\rangle$-transition. Cooler and repumper are not tuned on resonance but blue-shifted by a Δ of several linewidths. The repumper shift δ should be set as small as possible. The data was taken from [62].

cle and improve efficiency, but rather an indispensable element of the cooling scheme itself.

The setup that is used to produce the two desired frequencies is shown in Figure 4.10. The D_1 light is first shifted with a double pass using a 120 MHz acousto-optic modulator (AOM) with a bandwidth of 24 MHz (Gooch & Housego 3110-120). With this double pass setup, it is possible to control the blue detuning Δ by tuning the RF frequency that the AOM is driven with. Choosing an RF frequency of $f_{RF} = 94.45\,\mathrm{MHz}$ leads to a total shift of $f_{\mathrm{shift}} = 188.9\,\mathrm{MHz}$ after the double pass. In this case, the cooler is directly on resonance with the $|F = 2\rangle \rightarrow |F' = 2\rangle$-transition (see Figure 4.9). Choosing a higher RF frequency will lead to an additional blue detuning Δ. The highest accessible blue detuning with this setup is set by the maximum output of the RF driver at $f_{RF} = 150\,\mathrm{MHz}$. In this case, the resulting blue detuning is $\Delta = 2 \cdot f_{RF} - 188.9\,\mathrm{MHz} = 111.1\,\mathrm{MHz}$. Since the linewidth of the sodium D_1 transition is $\Gamma = 9.76\,\mathrm{MHz}$ [62], this corresponds to $\Delta = 11.4\Gamma$.

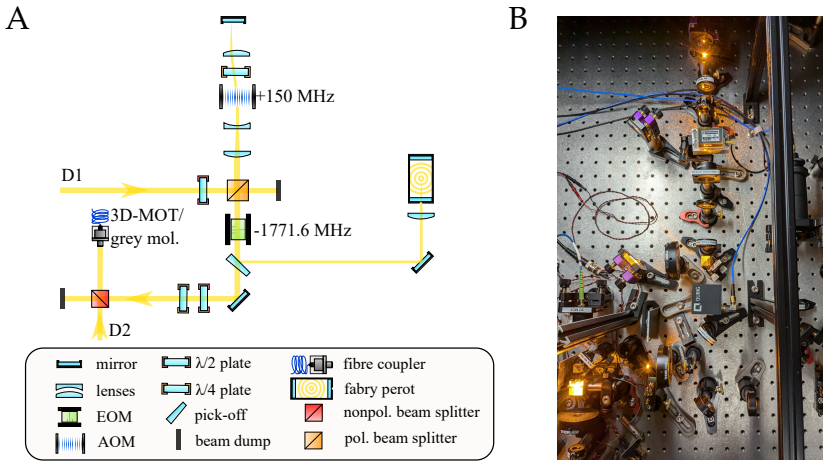

Figure 4.10.: Grey molasses optics setup.
A) A double pass shifts the cooler to the desired blue detuning. With the sideband of an EOM, the repumper is introduced. A Fabry-Perot interferometer is used to monitor relative cooler and repumper intensities. With a 50:50 beam splitter, the D_1 molasses light is overlapped with the D_2 MOT light.
B) Picture of the setup.

The spectroscopy is locked to the $|F = 2\rangle \rightarrow |F' = 1\rangle$-transition due to technical reasons. For the grey molasses typically a blue detuning in the range of 5Γ to 12Γ is desired. Since the lowest center frequency of AOMs for light in the VIS range is typically $f_{RF} = 80\,\mathrm{MHz}$, this range of blue detunings would not be accessible with a double pass setup if one would lock to the $|F = 2\rangle \rightarrow |F' = 2\rangle$-transition. However, if for some reason in the future, higher blue detunings are needed, one could also consider locking the SHG to the $|F = 2\rangle \rightarrow \mathrm{crossover}$. This would allow for blue detuning between 10Γ and 21Γ with the current setup. Even higher blue detunings could be possible if the AOM is swapped out with a different model with a higher center frequency.

The repumper mode is produced using an electro-optic modulator (EOM). When the EOM is switched on, it adds two sidebands to the original carrier frequency f_C. By driving the EOM with the frequency that corresponds to the hyperfine splitting of the groundstate ($f_{EOM} = 1771.6\,\mathrm{MHz}$) a sideband with the sum frequency $f_C + f_{EOM}$ and a sideband with the difference frequency $f_C - f_{EOM}$ is introduced. The difference fre-

quency sideband then acts as a repumper. The efficiency of the grey molasses is quite sensitive to this EOM shift. With the RF driver of the EOM, the repumper detuning δ (see Figure 4.9) can be controlled. The smaller δ is, the better does the grey molasses cool. The best cooling is achieved at $\delta = 0$ when the Raman condition is fulfilled.

After the EOM, a small portion of light is picked off and monitored with a Fabry-Perot interferometer (Thorlabs SA200-5B). The relative intensity of the cooler and repumper I_C/I_R can be determined by comparing the relative intensities of the transmission maxima of the interferometer (see Figure 4.17). This relative intensity can be tuned with the RF power that the EOM is driven with. The higher the RF power, the higher is the intensity in the sidebands.

A mirror, two λ-plates, and a 50:50 beam splitter are used for polarization-maintaining coupling. The beam splitter is used for overlapping the D_1 grey molasses beam with the D_2 3-MOT beam (see also Figure 4.4) since they share a fiber to the experimental table. This is due to the fact that the grey molasses uses the MOT optics on the experimental table. Shutters before the 50:50 beam splitter are used to switch between the two light sources for the different cooling stages. The optimization of the grey molasses in the following section was done with 90 mW of laser power arriving at the experimental table.

4.3. Optimization and Characterization

4.3.1. Microwave Spectroscopy

As explained in Section 4.1, it is preferable if the grey molasses is operated with three energy levels only, with little other energy levels in proximity that mix into the dark state. Therefore, I aimed to avoid Zeeman splitting as much as possible during the first optimization of the grey molasses. In our setup this is mitigated with three offset coils for the east-west (EW), north-south (NS) and top-bottom (TB) directions. The design for the power supplies of these coils was recently improved by Pirmin Adam. His new bidirectional design allows for switching the polarities of the coils throughout the sequence. The version that was used in the following sections is attached in Appendix B. It helped optimize the grey molasses, whose optimal offset currents have a different polarity from the optimal offsets for other stages of the experiment. An updated version of the design is currently being produced and tested.

One way to probe and minimize the magnetic field in the atom sample is by employing microwave spectroscopy (MS). Here, the sodium atoms are first cooled. In our sequence with a MOT, magnetic trap and microwave evaporation in the magnetic trap were used. They are then loaded into a cODT. This ensures that there is little Doppler broadening during the spectroscopy. In the magnetic trap, atoms in the $|F = 1, m_F = -1\rangle$ state of the sodium ground state are captured. During the spectroscopy, a microwave pulse at a frequency f_{MW} slightly below the zero-field resonance for the $|F = 1\rangle \rightarrow |F' = 2\rangle$ transition is used to pump atoms into the $|F = 2\rangle$ manifold of the ground state. The possible transitions that can occur due to this pulse are shown in Figure 4.11 A. At the end of the Sequence, the $|F' = 2\rangle$ atoms are blown away with resonant light such that only $|F = 1\rangle$ atoms remain. The process is then repeated several times for different microwave frequencies. If there is a magnetic field present, three dips in atom number should appear whose separation Δf_{MW} should correspond to the Zeeman splitting via $\Delta E = h \cdot \Delta f_{MW} = \mu_B B$.

In Figure 4.11 B the optimization process for the top-bottom coil is shown. At first, a scan with no compensating offset fields shows a separation of the atom number dips of approximately $\Delta f_{MW} = 0.3\,\mathrm{MHz}$. This corresponds to a magnetic field strength in the sample of $B = h \cdot \Delta f_{MW}/\mu_B = 214\,\mathrm{mG}$. The top-bottom coil current is then incrementally increased until the observed dips stop moving closer together and start diverging again. Then the same process is repeated for the next two coils until all

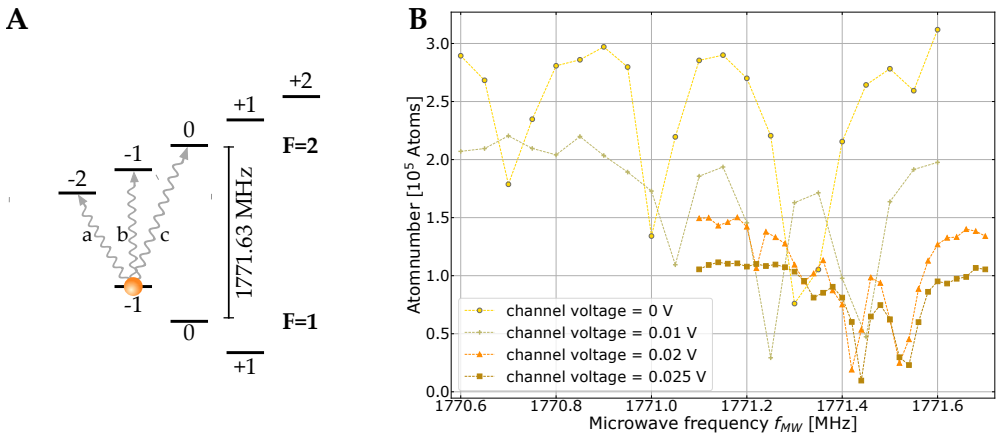

Figure 4.11.: Working principle of microwave spectroscopy with sodium.
A) Hyperfine level diagram of the ground state of sodium when a magnetic field is present. From the $|F = 1, m_F = -1\rangle$ ground state three transitions to the $|F' = 2\rangle$ manifold with $\Delta m_F = -1, 0, 1$ labeled with a, b, and c respectively are allowed. The transition frequencies correspond to $f_a = 1771.6 - 3\mu_B B/h$, $f_b = 1771.6 - 2\mu_B B/h$ and $f_c = 1771.6 - \mu_B B/h$ if the linear Zeeman effect is taken into account. The Figure was taken from [30].
B) Optimization of the top-bottom offset coil using microwave spectroscopy. By increasing the channel voltage controlling the current in the offset coil, the magnetic field in the atom sample can be compensated. When approaching the right offset field, the atom number dips should move closer together and shift closer to the zero field prediction.

dips coincide in one valley that should sit at the zero field prediction of the hyperfine splitting which in our case is $f_{HF} = 1771.63\,\mathrm{MHz}$. With this approach, a first optimization of the offset currents was done before tackling the molasses parameters. When the first molasses signal was detected, the offset currents were fine-tuned on the molasses signal. The first optimization process of the grey molasses after installing the new bidirectional power supplies is described in the following section.

4.3.2. Molasses Parameters

When optimizing a cooling stage of a cold atom experiment, one should simultaneously optimize the atom number and the reached temperature of the atom cloud. Both are important for condensation as the ultimate goal is reaching a sufficient phase space density $\rho = n\lambda_{dB}^3$. Here, n is the atom number density and λ_{dB} the thermal deBroglie

wavelength. It is therefore important to conserve as many atoms as possible while cooling them as low as possible.

Atom numbers in cold atom clouds can be estimated with a single absorption image. The thermal atom cloud that is transferred to the grey molasses from the MOT has a Gaussian density distribution originating from the combined effects of the trapping potential in the MOT and the thermal occupation of energies according to Bose-Einstein statistics [35] [63]. Atom numbers of thermal clouds can therefore be estimated by fitting a two-dimensional Gaussian with width $\sigma_{x,y}$ to the absorption image of the atom cloud. This fit is then used as an intensity distribution which estimates the atom number using Beer-Lambert's law, given by the relation

$$I_{x,y} = I_0 e^{-n(x,y)\sigma_{eg}}, \tag{4.18}$$

where $I_{x,y}$ is the Gaussian fit to the measured transmitted intensity, $n(x, y)$ is the column density of the atom number and σ_{eg} is the absorption cross-section. The atom number is found by integrating the column density $n(x, y)$. For more information on our absorption imaging scheme, one can consult [30].

Measuring the temperature of a cold atom cloud requires taking several absorption images. In a time of flight (TOF) measurement the atoms are allowed to expand freely for a time t before the atom cloud is imaged. During this time, thermal atom clouds will expand, since there is no potential confining them anymore. One can use this thermal expansion to estimate the temperature after the cooling stage by measuring the Gaussian width $\sigma_{x,y}$ for different time of flights after the cooling stage. The hotter the atom cloud is, the quicker it expands. Assuming a ballistic expansion, the relation between the width at a time t and the temperature $T_{x,y}$ is given by

$$\sigma_{x,y}^2(t) = \sigma_{x,y}^2(0) + \frac{k_B T_{x,y}}{m} t^2 \tag{4.19}$$

Here, k_B is the Boltzmann constant and m the atomic mass. The temperature of the atom cloud can therefore be obtained by performing a linear fit of $\sigma_{x,y}^2(t)$ versus t^2 [35] [30].

For a quicker optimization however, where the absolute temperature is not as important as the relative change in temperature that occurs when varying the optimized

parameter, it is impractical to perform TOF measurements for every single change of the optimization parameter in the scan. Here, the width of the atom cloud after one long TOF can act as a crude estimator for temperature. Scanning the parameter that needs to be optimized two to four times helps estimating the magnitude of fluctuations. With this method most of the following optimizations were performed.

From one measurement of the atom cloud width alone is not possible to perform a linear fit to yield an absolute temperature. To better interpret the optimization data that is presented in the following section, I used some TOF measurements that were performed after the optimization process to extrapolate an approximate width of the atom cloud for $t = 0$ (see Figure 4.18). This was then used as a second width for a linear temperature fit for the optimization data. The temperature values given in Figures 4.12-4.16 should therefore not be interpreted as very accurate measures but rather as rough estimates of the order of magnitude of the reached temperatures and relative temperature changes. The proper TOF measurements that were performed after the optimization are the much more precise temperature measurements.

Having this in mind, I still believe there is value in understanding how much impact which parameter roughly has on atom number and temperature, while also not spending too much time on doing lots of TOF measurements for the single species grey molasses when the more important mode of operation includes both species. In the following sections, a single-species optimization process of the sodium grey molasses is presented and the effects of important parameters on the grey molasses are discussed. If in the future dual-species condensation can be achieved utilizing grey molasseses for sodium and potassium, it might be worthwhile to properly characterize the molasses stage with TOF and phase space density measurements.

Raman condition

The first most sensitive condition that has to be fulfilled to be able to see a grey molasses is the Raman condition. As mentioned in Section 4.2.3, the repumper detuning δ (see Figure 4.9) has to be as small as possible for the grey molasses to work.

In Figure 4.12 a typical dependency of the molasses temperature on different repumper detunings is shown. For $\delta < 0$ grey molasses cooling is observed. The most efficient cooling occurs for detunings close to zero where the Raman condition is best fulfilled. For $\delta > 0$, significant heating occurs. In this case, it becomes more likely to motionally

couple to bright states which have a potential maximum at the position that the atoms were coupled. They then wander down the potential hill and are subsequently heated instead of cooled. A good explanation of this phenomenon can be found in [64] where the eigenstates of rubidium atoms in a D_2 grey molasses were calculated numerically for the cases $\delta < 0$ and $\delta > 0$.

The repumper detunings can be tuned by varying a microwave frequency that is applied to an EOM (see Section 4.2.3). The Raman condition should theoretically be met when a frequency of $f_{EOM} = 1771.63\,\mathrm{MHz}$ is applied which corresponds to $\delta = 0$ in Figure 4.12. The temperature minimum, however, does not always perfectly coincide with the literature value. In our case, the optimal value was found closer to $f_{EOM} = 1771.93\,\mathrm{MHz}$ or $\delta = 0.3\,\mathrm{MHz}$. This shift could be due to some finite residual magnetic field. Another possibility could be a miscalibration of the microwave source.

The atom number in the grey molasses is also significantly affected by the Raman condition. For positive detunings, where heating occurs, the atom number quickly declines. For detunings as small as $\delta = 1.3\,\mathrm{MHz}$, the atom number is already consistent with zero. During the grey molasses, the atoms are not trapped and only cooled. If done right, this is not detrimental since the duration of this cooling stage is kept short. If the sample is too hot though, high atom losses can be expected during this stage. This is especially true if the grey molasses does not mitigate the thermal expansion well enough by cooling, as is the case for positive detunings. For small negative detunings, the atom number exhibits a plateau.

The optimal choice for the EOM frequency which sets the repumper detuning is therefore at the detunings with minimal temperature. Here, the atom number should still lie within the high plateau. For this parameter, no trade-off needs to be made between atom number and temperature which is not the case for all grey molasses parameters. In dual-species operation, the Raman condition of each single-species should also not be affected by the presence of the other species. Before trying to optimize both species together it therefore might be helpful to first find the single-species Raman conditions respectively and then start optimizing the other parameters on both species.

Generally, the Raman condition should be the first point of optimization (regarding the software-controlled non-optics elements). If the Raman condition is not sufficiently fulfilled, attempts to optimize other parameters should not yield good results.

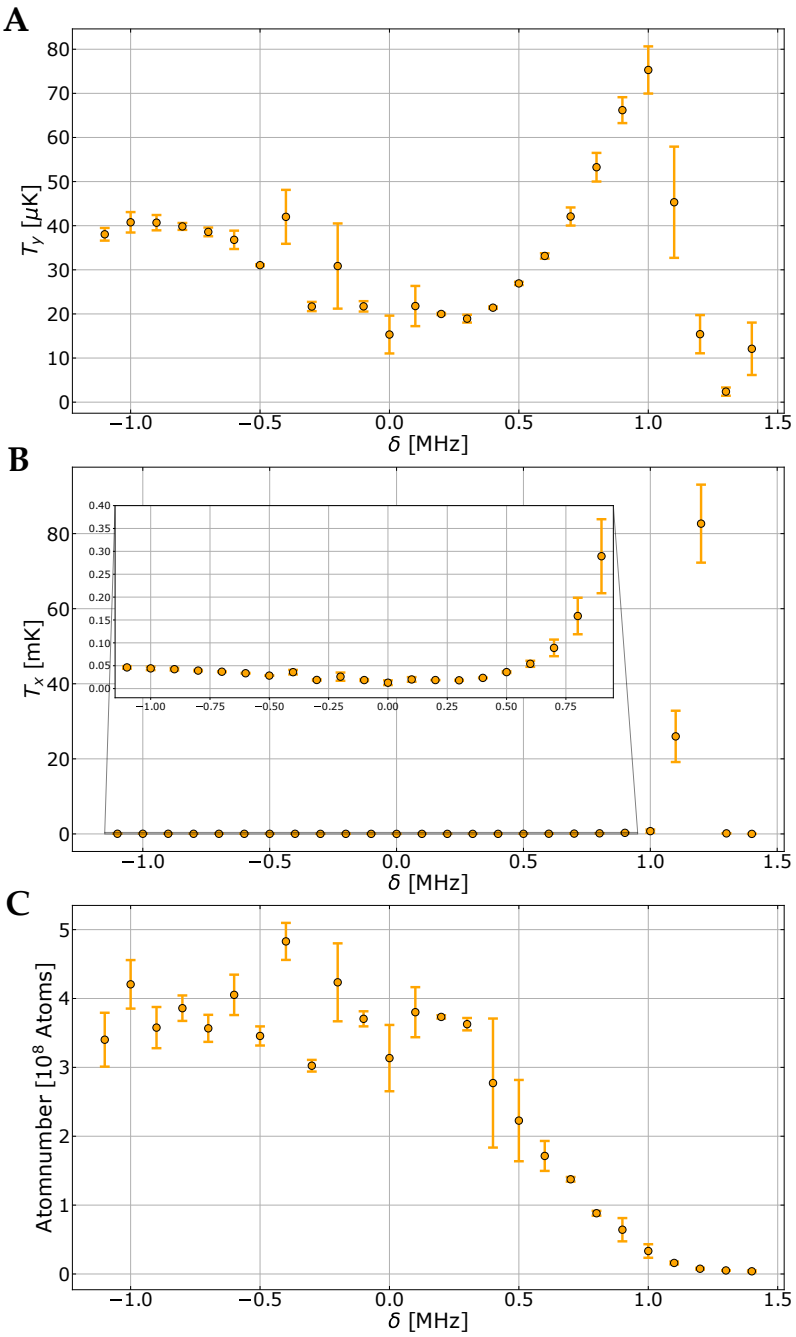

Figure 4.12.: Optimization scan of the Raman condition in single-species operation of the D_1 grey molasses. The repumper detuning δ was varied by changing the microwave frequency applied to an EOM which creates the repumper as the difference sideband to the cooler. $\delta = 0$ corresponds to the literature value for the groundstate hyperfine splitting $f_{EOM} = 1771.6\,\mathrm{MHz}$ [62].
A, B) Temperature as a funciton of the repumper detuning. From the two-dimensional Gaussian fit to the thermal cloud, two temperatures can be calculated with Equation (4.19).
C) Atom number as a function of the repumper detuning. For negative detunings, the atom number exhibits a plateau. For positive detunings, the atom number quickly drops off to zero.

Changing the blue detuning, hold times and cooler-repumper ratio should not impact the optimal EOM frequency for meeting the Raman condition. After changing offset fields, it is however advisory to check the Raman condition again because the offset fields impact the energy differences between the addressed transitions. The measurement that is presented in Figure 4.12 was done after a fine-tuning of the offset fields on an already working grey molasses.

Offset fields

Even though using the microwave spectroscopy for zeroing the magnetic field during the molasses (see Section 4.3.1) is a helpful first guess for finding a molasses that is not working, optimizing on the molasses itself (if possible) is always preferable. While the values that were found with the microwave spectroscopy ($U_{TB} = 0.35\,\mathrm{V}$, $U_{EW} = -0.025\,\mathrm{V}$, $U_{NS} = 0\,\mathrm{V}$) were close enought to the optimum for finding a first Raman condition and a first rather hot grey molasses, they were not optimal.

In Figure 4.13, an example of the successive optimization of the channel voltages of the offset coils is shown. The atom number is mostly unaffected when scanning this parameter in these ranges, but the molasses temperature could be reduced by several 10s of microkelvins. This was also partly due to the fact that for the data presented in Figure 4.13, the other parameters were mostly unoptimized and the molasses was therefore hot to begin with. Depending on where in parameter space one is sitting when one conducts this measurement, the absolute effect on the temperature might be smaller or larger. The dependency of the temperature on the offset field should however still show the same U-shape.

After selecting the offset channel voltage for which the temperature is minimized, one should reoptimize the Raman condition before moving on to other parameters. Deducing from the data in Figure 4.13, the offset channel voltages were set to $U_{TB} = 0.2\,\mathrm{V}$, $U_{EW} = 0\,\mathrm{V}$, $U_{NS} = 0.08\,\mathrm{V}$. While these might be the optimal values in single-species operation, one has to keep in mind that the offset fields impact both species. In might not be true that these values are still optimal in dual-species operation. It might also be the case that in dual-species operation atom numbers are affected more severely by the offset fields. This parameter definitely needs to be revisited in the dual-species optimization.

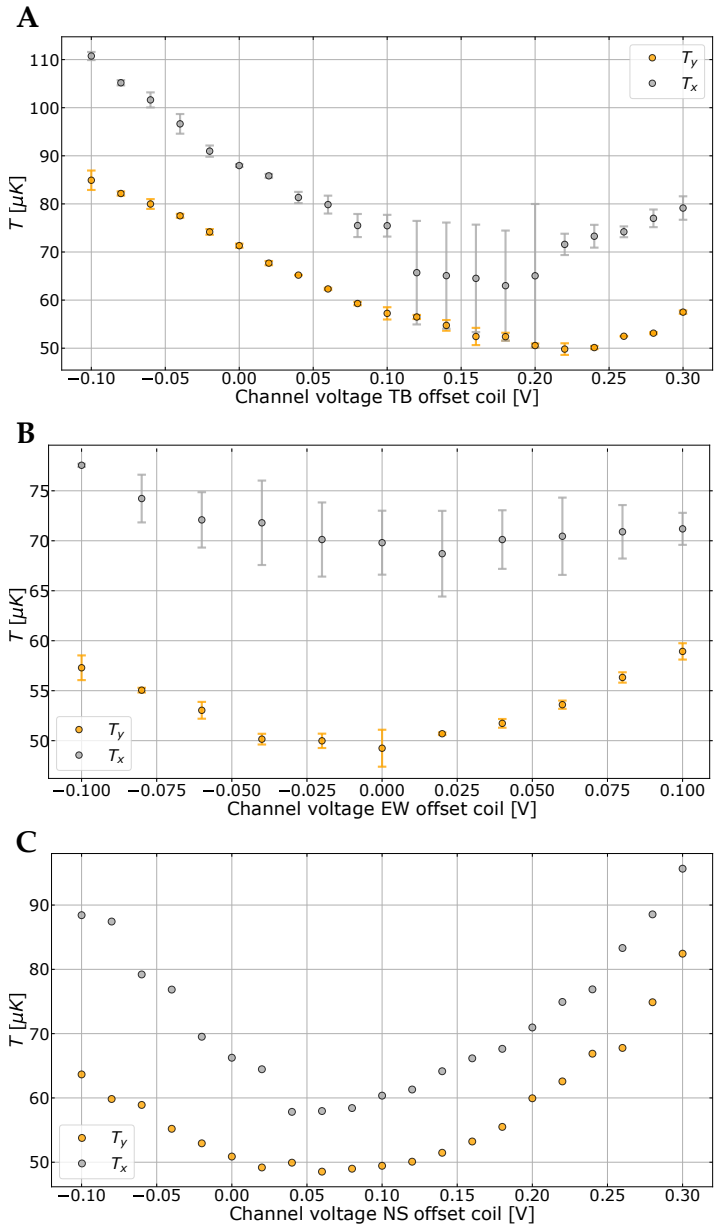

Figure 4.13.: Optimization scan of the offset coil channel voltages in single-species operation of the D_1 grey molasses.
A, B) The top-bottom coil has a big impact on the molasses temperature and has to compensate for the largest magnetic field out of all three coils. The east-west coil on the opposite shows a shallow temperature minimum for zero offset current.
C) For optimizing the north-south offset coil only one set of data was taken. Because the temperature minimum for this coil was abundantly clear after one scan, no additional scans were taken to account for fluctuations.

Blue detuning

The blue detuning Δ can be controlled by applying a Voltage U_{VCO} to an RF driver containing a VCO. The driver is used to provide an RF signal to the AOM which shifts the D_1 frequency in the grey molasses double pass (see Section 4.2.3). The frequency of this RF signal is proportional to U_{VCO} (see Figure 4.14).

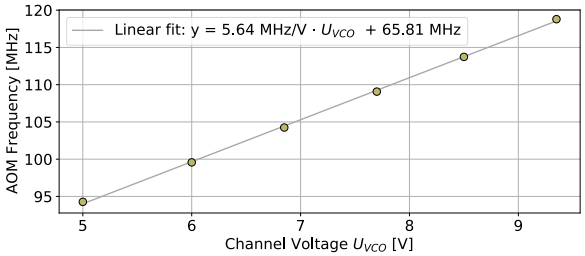

Figure 4.14.: Grey molasses double pass AOM frequency as a function of the Channel voltage U_{VCO} applied to the VCO in the RF driver.

With the experiment control a maximum of 10 V can be applied to the RF driver externally. The maximal blue detuning that can be reached with this external voltage is $\Delta = 55\,\mathrm{MHz} = 5.65\Gamma$ (meaning $f_{AOM} = 122\,\mathrm{MHz}$). In Figure 4.15, the relationship between temperature and blue detuning and atom number and blue detuning is shown for the highest blue detunings that are accessible with the experiment control. While the atom number is not notably affected, the temperature slowly but significantly drops for higher blue detunings.

Judging from this measurement, it seemed reasonable to switch from driving the RF driver externally to using the internal setting. This allows for higher VCO voltages and therefore higher RF frequencies and blue detunings. Currently, the grey molasses is operated with the maximal RF frequency that the driver provides. This leads to an AOM frequency of $f_{AOM} = 150\,\mathrm{MHz}$ and a blue detuning of $\Delta = 111\,\mathrm{MHz} = 11.4\Gamma$.

If one wants to explore the effects of higher blue detunings in the future one could consider changing the lockpoint as described in Section 4.2.2. When changing the AOM frequency by a large amount, one has to keep in mind that the changed angle after the AOM could lead to clipping at the iris after the AOM that selects the first order. The reduced laser power arriving at the atoms as a result of this could lead to a reduced efficiency of the molasses. After big changes of the AOM frequency, one should therefore check the double pass efficiency and tweak the setup if needed.

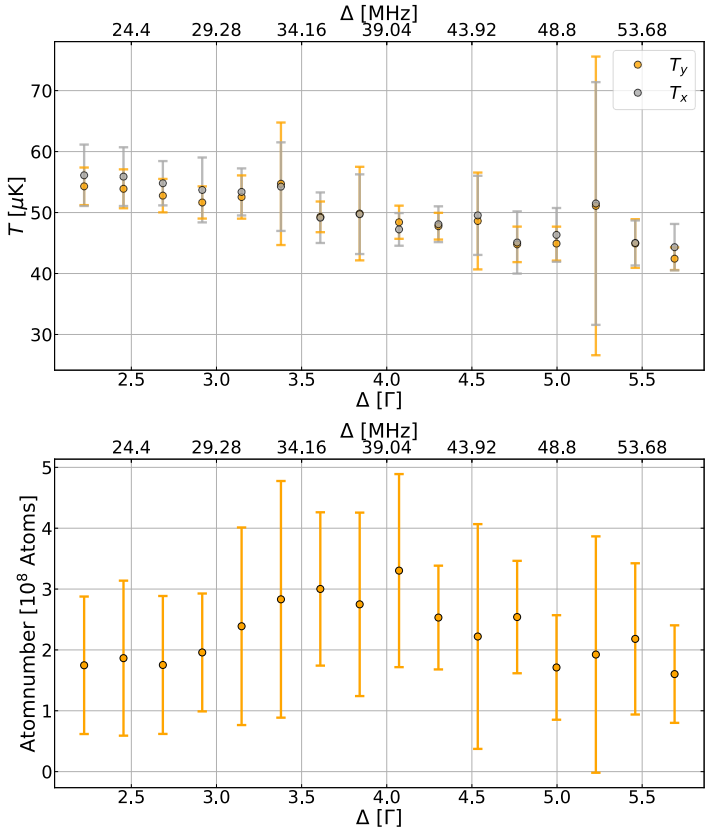

Figure 4.15.: Grey molasses temperature and atom number as a function of blue detuning in single-species operation of the D_1 grey molasses. The atom number is mostly unaffected, while the temperature decreases for higher blue detunings.

Hold times

When optimizing the hold time of the grey molasses, a trade-off between atom number and temperature has to be made. During the molasses, the atoms are not trapped or "held" as the naming of the "hold time" suggests. They expand thermally as they are cooled and have to be recaptured after the molasses. The measurement in Figure 4.16 shows that as the atom number goes down considerably for longer grey molasses times, so does the temperature.

It is probably most useful to optimize this parameter in later stages of the experiment when one is already condensed or close to condensing. Then it can be helpful to tweak this parameter while optimizing the condensed fraction. Only looking at the grey molasses, it is not necessarily clear what the best trade-off between atom number and temperature is for the final sample.

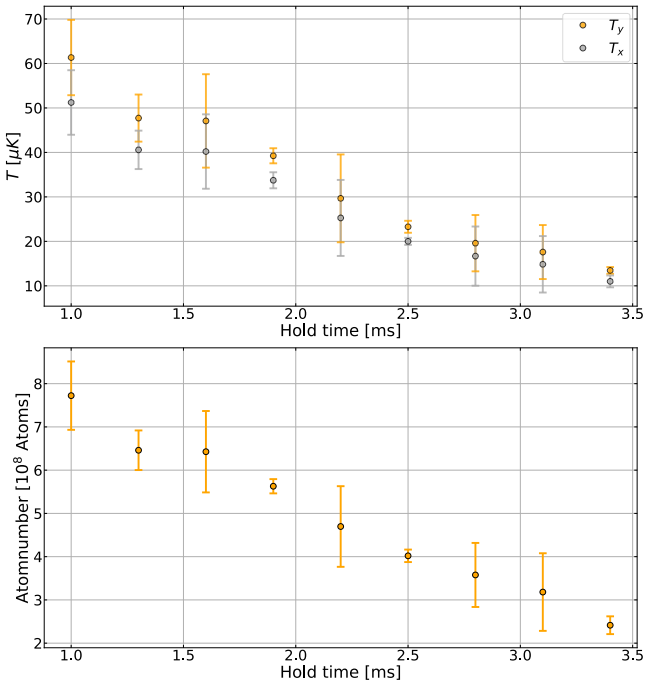

Figure 4.16.: Grey molasses temperature and atom number as a function of molasses hold time in single-species operation of the D_1 grey molasses. Both show an inverse relationship with hold time. Since both low temperatures and high atom numbers are desired, a tradeoff between atom number and temperature has to be made.

Cooler-Repumper ratio

The cooler-repumper ratio can be tuned by changing the power of the microwave signal that is applied to the EOM. A higher power results in more intense sidebands and therefore more repumper power compared to the cooler power. The ratio can be determined with the Fabry-Perot signal (see Figure 4.17). The current ratio that the grey molasses is operated with is $I_R/I_C = 28.92\%$.

In the future, it might be interesting to experiment with different cooler-repumper ratios to determine the effects on the grey molasses. A slight reconstruction of the experiment would be needed to make this possible. Around the power that the microwave source currently operates, it is not possible to tune the amplitude smoothly. Before making a cooler-repumper ratio measurement one should make sure, that the microwave source operates at a lower power where tuning the power is possible without large jumps and amplify the signal afterwards before sending it to the EOM. When the signal is changed, one should make sure that the resonance condition of the EOM is still met and the damage threshold of the EOM is not exceeded.

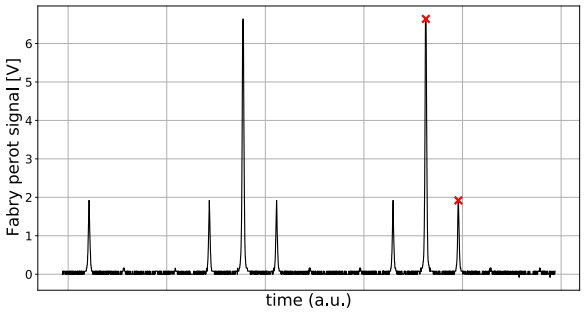

Figure 4.17.: Fabry-Perot signal picked off after the EOM, showing the spectrum of the grey molasses light. The more intense peaks correspond to the carrier (cooler) mode, while one of the less intense sideband peaks is used as the repumper. By finding the peak positions (indicated with red crosses) and amplitudes of the peaks, one can find the cooler-repumper ratio by dividing the carrier amplitude by the sideband amplitude.

Molasses temperature

After the optimization process that was presented in the previous sections, three time of flight measurements were conducted for measuring the temperature of the sample after the grey molasses stage. Using equation (4.19), the temperature of the sample was found by performing a linear fit to the mean of the three measurements.

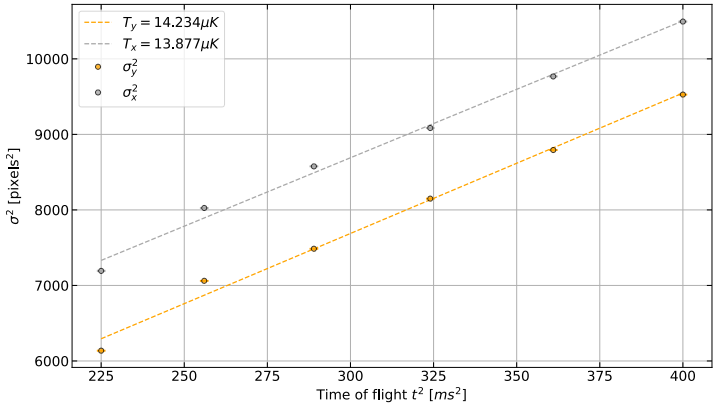

Figure 4.18.: Squared widths of the atom clouds as a function of the squared time of flight after the optimized grey molasses. A mean of three measurements was used to perform a linear fit, which yields the molasses temperature according to Equation (4.19). With the parameters of this fit, approximate widths $\sigma_{x,0}$ and $\sigma_{y,0}$ for $t = 0$ could be extrapolated. They could then be used as a second width for a linear temperature fit for the optimization data in Figures 4.12-4.16.

From the thermal expansion in x- and y-direction, the temperatures $T_x = 13.9\,\mu\text{K}$ and $T_y = 14.2\,\mu\text{K}$ could be deduced respectively. This is comparable to the temperatures that were historically achieved with a microwave evaporation in the magnetic trap ($T_{MW} = 10\,\mu\text{K}$ [30]). The atom number $N_{GM} = 5 \times 10^8$ after the grey molasses however is several orders of magnitude larger than the atom number after the microwave evaporation ($N_{MW} = 5 \times 10^5$ [30]). It is also likely underestimated due to the grey molasses being too dense for the absorption imaging after optimization. Compared to the bright MOT temperature $T_{MOT} \approx 400\,\mu\text{K}$, two orders of magnitude could be won, while $N_{GM}/N_{MOT} \approx 80\%$ of the atoms were conserved.

In Table 4.2, the set of parameters with which this temperature was achieved is listed. In single-species operation, it was possible to condense sodium using the grey molasses instead of a microwave evaporation. First attempts of condensing in dual-species operation yielded a cold sample in the dipole trap at the end of the dipole evaporation which contained $N_{Na} = 1.85 \times 10^4$ sodium atoms and $N_K = 3.74 \times 10^3$ potassium atoms (see Figure 4.19). Albeit dual-species condensation not being achieved yet, it seems plausible that with some more optimization, a dual-species condensate could be realized with the help of the grey molasses.

Table 4.2.: Chosen parameters for the single-species grey molasses after the presented optimization process

Parameter	Value
NS coil channel voltage	0.08 V
EW coil channel voltage	0 V
TB coil channel voltage	0.2V
EOM frequency (Raman condition)	1771.9 MHz
AOM frequency	150 MHz
Blue detuning	111 MHz = 11.4 Γ
Hold time	2.5 ms
Cooler-repumper ratio	28.92%
Laser power on experimental table	90 mW

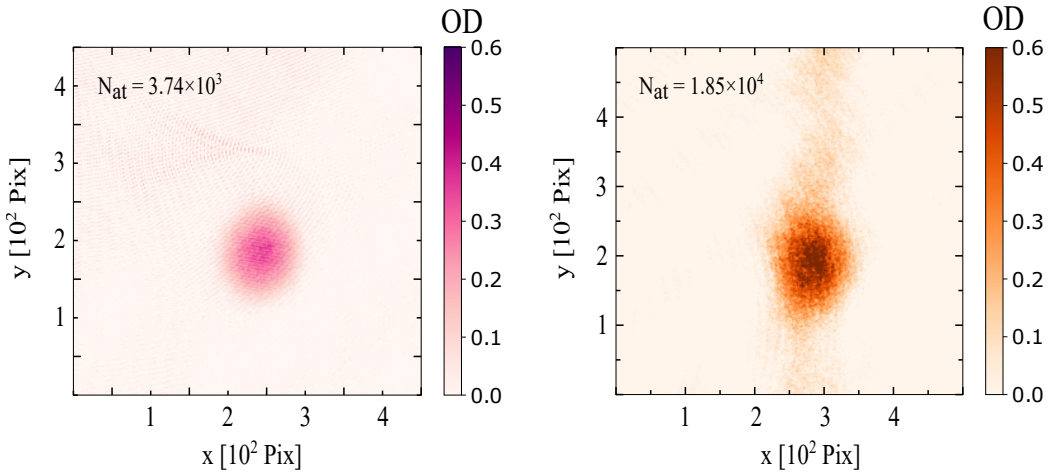

Figure 4.19.: Potassium (left) and sodium (right) atom clouds imaged at the end of a dipole evaporation. The cooling sequence included the newly implemented sodium grey molasses.

CHAPTER 5

Conclusion and Outlook

5.1. Summary

In this thesis, advancements in both the potassium and sodium setups for the dual-species SoPa experiment are presented. The potassium high-field imaging system facilitates the imaging of potassium atoms at later stages of the experimental sequence when Feshbach fields are applied. Optical and electronic components for implementing an offset beat lock were assembled, achieving a stable lock. Additionally, theoretical predictions for the required offset frequencies at various Feshbach fields were computed numerically. The high-field imaging light has been coupled into the imaging fibers leading to the experimental table and is ready for testing in the experiment.

Furthermore, several alterations to the sodium laser table were performed. By replacing a Toptica SHG with a more powerful fiber laser, the setup for the sodium 2D-MOT, 3D-MOT, and imaging light could be simplified. The Saturated Absorption Spectroscopy for locking the fiber laser was rebuilt with a newer spectroscopy cell. With the same spectroscopy, the SHG unit was locked to the D_1 line of sodium. Using the SHG light, a new optics setup for a sodium grey molasses was implemented.

The D_1 grey molasses for sodium will hopefully prove as a valuable stepping stone towards dual-species condensation. It was able to replace the previously used microwave evaporation which limited the experiment due to high losses of atoms. Temperatures as low as $T = 14\,\mu\mathrm{K}$ could be reached consistently with the molasses. Compared to the microwave evaporation a higher percentage of atoms could be conserved. Single-species condensation has already been achieved using the new grey molasses setup and attempts at dual-species operation were promising. The condensation of both species together will hopefully only be a matter of time.

5.2. Outlook

Following dual-species condensation, there are three main milestones that need to be reached before the SoPa experiment functions as a quantum simulator. After condensation, the atoms will be loaded into a two-dimensional optical trap (2D trap). Here, the atoms are tightly confined along one direction, leading to a quasi two-dimensional system. The atoms which are spread across the horizontal plane should then be imaged vertically. This high-resolution imaging setup was planned and characterized by Lilo Höcker [31] and will be implemented soon after dual-species condensation was achieved.

Once the 2D-trap and vertical imaging setup are installed, first measurements of demixing dynamics in two dimensions can be employed. The needed fields and sequences for preparing impurities, mixtures, condensed coarse or fine domains, and the effects of buoyancy can be investigated.

Finally, a method for creating potential landscapes that the atoms experience during simulation needs to be planned and realized. Digital Micromirror Devices (DMDs) are a versatile and commonly used tool for imprinting potentials using light fields [16,49,65]. Once a reliable method for shaping the potentials in the simulated Hamiltonians is implemented, the SoPa experiment is fully equipped to tackle fundamental questions about the nature surrounding us.

APPENDIX A

Potassium Zeeman Shift Calculation

Calculation of the needed offset frequency for imaging ^{39}K at an offset field of 160 G.

```
import numpy as np
import matplotlib.pyplot as plt
from scipy.linalg import eig
import matplotlib
import itertools
font = {'family' : 'normal',
            'weight':'normal',
        'size'   : 17}
from scipy.constants import h as h_Planck
from scipy.constants import physical_constants
mu_B = physical_constants['Bohr magneton'][0]

# numbers for Sodium
dHFS_Na = 1.7716261288e9;gJ_Na = 2.002296; gI_Na = -0.00080461080;I_Na=3./2;

# numbers for K39
dHFS_K39 = 461.7e6;gJ_K39 = 2.00229421; gI_K39 = -0.00014193489;I_K39=3./2;
spectroscopy_shift = 57.75

def get_breit_rabi_energy(mag_field_B, nuclear_moment_I, g_I, g_J, d_hfs,
    nuclear_spin_F, m_F):
    '''GetBreitRabiEnergy  Calculate the spectrum according the Brei-Rabi
        equation
    B0    magnetic field in T
    I     nuclear moment
    '''
    E1 = g_I*mu_B*m_F*mag_field_B;
    x = (g_J-g_I)*mu_B*mag_field_B/h_Planck/d_hfs;
    E2 = -h_Planck*d_hfs/2.*np.sqrt(1+4*m_F*x/(2.*nuclear_moment_I+1)+x**2);
    if nuclear_spin_F==1:
        E_tot =  E1 + E2;
    elif nuclear_spin_F==2:
        if m_F==-2:
```

```
32            # In this case the argument in the square root becomes negative,
                  which is why we need an approximation for this state
33            E_tot =  E1 + h_Planck*d_hfs/2.*(1-x)
34        else:
35            E_tot =  E1 - E2;
36    return E_tot
37
38 def diagD2excited(B):
39    # Constants from Rev.Mod.Phys. 49,31 (1977)
40    Ahfs = 6.093               #MHz
41    Bhfs = 2.786               #MHz
42    gJ = 4/3
43    gI = -0.00014193489
44    muB = 1.3996245042*10000   #MHz/Tesla
45    ge = 2.00231930436182
46
47    I = 3/2
48    J = 3/2
49
50    # Define I and J matrices
51    Iz = np.diag(np.tile(np.arange(-3/2, 4/2), 4))
52    temp = np.tile(np.append(np.sqrt((3/2 - np.arange(-3/2, 3/2)) * (3/2 + np.
          arange(-3/2, 3/2) + 1)), 0), 4)
53    Ip = np.diag(temp[:-1], -1)
54    temp = np.tile(np.insert(np.sqrt((3/2 + np.arange(-3/2 + 1, 4/2)) * (3/2 - np
          .arange(-3/2 + 1, 4/2) + 1)), 0, 0), 4)
55    Im = np.diag(temp[1:], 1)
56    Ix = 0.5 * (Ip + Im)
57    Iy = 0.5j * (Ip - Im)
58
59    Jz = np.diag(np.concatenate([np.repeat(-3/2, 4), np.repeat(-1/2, 4), np.
          repeat(1/2, 4), np.repeat(3/2, 4)]))
60    temp = np.sqrt((3/2 - np.arange(-3/2, 3/2)) * (3/2 + np.arange(-3/2, 3/2) +
          1))
61    temp = np.concatenate([np.repeat(temp[0], 4), np.repeat(temp[1], 4), np.
          repeat(temp[2], 4), [0]])
62    Jp = np.diag(temp[:-1], -4)
63    temp = np.sqrt((3/2 + np.arange(-3/2 + 1, 4/2)) * (3/2 - np.arange(-3/2 + 1,
          4/2) + 1))
64    temp = np.concatenate([[0], np.repeat(temp[0], 4), np.repeat(temp[1], 4), np.
          repeat(temp[2], 4)])
65    Jm = np.diag(temp[1:], 4)
66    Jx = 0.5 * (Jp + Jm)
```

```
    Jy = 0.5j * (Jp - Jm)

    # Hyperfine interaction and Zeeman term
    IJ = (Ix @ Jx + Iy @ Jy + Iz @ Jz)
    Hhfs = Ahfs * IJ + Bhfs * (3 * IJ**2 + 1.5 * IJ - I * (I + 1) * J * (J + 1) *
         np.diag(np.ones(len(Jz)))) / (2 * I * (2 * I - 1) * J * (2 * J - 1))

    # Magnetic field term
    HB = muB * (gI * Iz + gJ * Jz) * B
    H = Hhfs + HB

    # Eigenvalues and eigenvectors
    EigenVals, V = np.linalg.eigh(H)

    #JzVec = np.diag(Jz)
    #IzVec = np.diag(Iz)

    return EigenVals, V

def offset_lock_shift(B):
    excited_shift_Zeeman = diagD2excited(B)
    ground_shift_Zeeman = get_breit_rabi_energy(B, I_K39, gI_K39, gJ_K39,
        dHFS_K39, 1, -1)/h_Planck*1e-6
    spectroscopy_shift = 57.75 - 2.1
    cooler_shift = 231

    return (excited_shift_Zeeman[0][2] - ground_shift_Zeeman - spectroscopy_shift
         - cooler_shift)

# Magnetic field
magnetic_field_max = 180e-4 # magnetic fields up to 180G
num_points = 1000
Bs = np.linspace(0, magnetic_field_max, num_points)

# Initialize the energy array
energies = {}
for atom in atoms:
    for F in nuclear_spins:
        energies[(atom, F)] = np.zeros((num_points,2*F+1))


# Calculate energy levels ground state
atoms = ['Na', 'K39']
```

```
nuclear_spins = [1, 2]

for atom in atoms:
    for F in nuclear_spins:
        # Constants specific to each atom
        if atom == 'Na':
            nuclear_moment_I = I_Na
            d_hfs = dHFS_Na
            g_I = gI_Na
            g_J = gJ_Na
        elif atom == 'K39':
            nuclear_moment_I = I_K39
            d_hfs = dHFS_K39
            g_I = gI_K39
            g_J = gJ_K39

        # Calculate energy levels
        for ii in range(2*F+1):
            m_F = -F + ii
            energies[atom, F][:, ii] = get_breit_rabi_energy(Bs, nuclear_moment_I
                , g_I, g_J, d_hfs, F, m_F)

#Calculate energy levels excited state
excited_energies = []

for j in Bs:
    excited_energies.append(diagD2excited(j)[0])

excited_energies = np.array(excited_energies)
excited_energies = excited_energies.T

# Plot energy levels
fig, (ax1, ax2) = plt.subplots(2, 1, sharey=True, figsize=(15, 30))

for F in nuclear_spins:
    ax2.plot(Bs*1e4, energies['K39', F][:, :]/h_Planck*1e-6 - spectroscopy_shift,
         'r-')
    ax2.set_xlabel('$B_0$ [G]', fontsize=16)
    ax2.set_title('$^{2}S_{1/2}$ ground state splitting', fontsize=20)
    ax2.set_ylabel('E(MHz)', fontsize=16);
    ax2.set_ylim(-500, 400)
    ax2.set_xlim(0, 180)

```

```
148 ax2.plot(Bs*1e4, energies['K39', 1][:, 0]/h_Planck*1e-6 - spectroscopy_shift, 'k-
        ',  label=r'$|m_J, m_I \rangle = |-1/2, -1/2 \rangle $')
149 ax2.grid()
150 ax2.legend(fontsize=15)
151
152
153 for i in range(16):
154     ax1.plot(Bs*1e4, excited_energies[i], 'r-')
155     ax1.set_xlabel('$B_0$ [G]', fontsize=16)
156     ax1.set_title('$^{2}P_{3/2}$ excited state splitting', fontsize=20)
157     ax1.set_ylabel('E(MHz)', fontsize=16);
158     ax1.set_xlim(0, 180)
159
160 ax1.plot(Bs[30:]*1e4, excited_energies[2][30:], 'k-', label=r'$|m_J, m_I \rangle
        = |-3/2, -1/2 \rangle $')
161 ax1.plot(Bs[:28]*1e4, excited_energies[4][:28], 'k-')
162 ax1.plot(Bs[28:30]*1e4, excited_energies[3][28:30], 'k-')
163 ax1.grid()
164 ax1.legend(fontsize=15)
165
166
167 #label manifolds
168 ax1.text(100,375, r'$m_J = 3/2$',fontsize=15)
169 ax1.text(160,190, r'$m_J = 1/2$',fontsize=15)
170 ax1.text(160,-110, r'$m_J = -1/2$',fontsize=15)
171 ax1.text(160,-410, r'$m_J = -3/2$',fontsize=15)
172
173 #save figures
174 fig.savefig('BreitRabi_K.png', bbox_inches='tight');
175 fig.savefig('BreitRabi_K.pdf', bbox_inches='tight');
176
177 #Calculate offset lock shift
178 offset_lock_shift(160e-4)
```

APPENDIX B

Bidirectional Power Supply

Current iteration of the new bidirectional power supply. A newer version is being designed and soon to be tested.

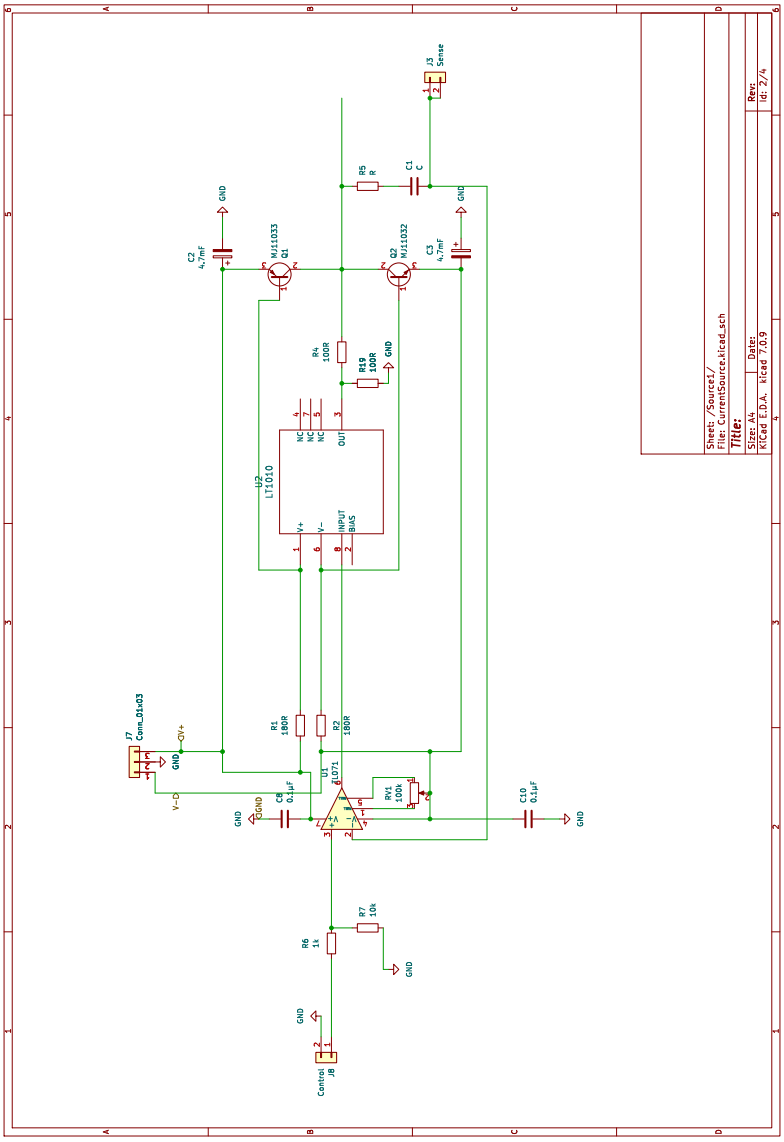

Figure B.1.: Pirmin Adam's preliminary bidirectional power supply design

List of Figures

List of Tables

Bibliography

[1] R. P. Feynman, "Simulating physics with computers," *International Journal of Theoretical Physics*, vol. 21, no. 6, pp. 467–488, 1982. (cited on page 1)

[2] S. Lloyd, "Universal quantum simulators," *Science*, vol. 273, no. 5278, pp. 1073–1078, 1996. (cited on page 1)

[3] G. E. Moore, "Cramming more components onto integrated circuits," *Electronics*, vol. 38, no. 8, April 19 1965. (cited on page 1)

[4] T. N. Theis and H.-S. P. Wong, "The end of moore's law: A new beginning for information technology," *Computing in Science Engineering*, vol. 19, no. 2, pp. 41–50, 2017. (cited on page 1)

[5] C. D. Bruzewicz, J. Chiaverini, R. McConnell, and J. M. Sage, "Trapped-ion quantum computing: Progress and challenges," 4 2019. (cited on page 1)

[6] R. Blatt and C. F. Roos, "Quantum simulations with trapped ions," *Nature Physics*, vol. 8, pp. 277–284, 4 2012. (cited on page 1)

[7] A. Trautmann, P. Ilzhoefer, B. Hochreiter, M. Mark, and F. Ferlaino, "Tweezer arrays for rydberg states in erbium for quantum simulation," in *APS Division of Atomic, Molecular and Optical Physics Meeting Abstracts*, ser. APS Meeting Abstracts, vol. 2020, Jan. 2020, p. Q01.161. (cited on page 1)

[8] R. Barends, J. Kelly, A. Megrant, A. Veitia, D. Sank, E. Jeffrey, T. C. White, J. Mutus, A. G. Fowler, B. Campbell, Y. Chen, Z. Chen, B. Chiaro, A. Dunsworth, C. Neill, P. O'Malley, P. Roushan, A. Vainsencher, J. Wenner, A. N. Korotkov, A. N. Cleland, and J. M. Martinis, "Superconducting quantum circuits at the surface code threshold for fault tolerance," *Nature*, vol. 508, pp. 500–503, 4 2014. (cited on page 1)

[9] C. M. Wilson, G. Johansson, A. Pourkabirian, M. Simoen, J. R. Johansson, T. Duty, F. Nori, and P. Delsing, "Observation of the dynamical casimir effect in a superconducting circuit," *Nature*, vol. 479, no. 7373, p. 376–379, Nov. 2011. (cited on page 1)

[10] C. G. Yale, B. B. Buckley, D. J. Christle, G. Burkard, F. J. Heremans, L. C. Bassett, and D. D. Awschalom, "All-optical control of a solid-state spin using coherent dark states," *Proceedings of the National Academy of Sciences*, vol. 110, pp. 7595–7600, 5 2013. (cited on page 1)

[11] R. LaPierre, *Solid-State Spin Qubits*. Cham: Springer International Publishing, 2021, pp. 259–273. (cited on page 1)

[12] M. H. Anderson, J. R. Ensher, M. R. Matthews, C. E. Wieman, and E. A. Cornell, "Observation of Bose-Einstein condensation in a dilute atomic vapor," *Science*, vol. 269, no. 5221, pp. 198–201, 1995. (cited on page 1)

[13] K. B. Davis, M. O. Mewes, M. R. Andrews, N. J. van Druten, D. S. Durfee, D. M. Kurn, and W. Ketterle, "Bose-Einstein condensation in a gas of sodium atoms," *Phys. Rev. Lett.*, vol. 75, pp. 3969–3973, Nov 1995. (cited on page 1)

[14] S. Inouye, M. R. Andrews, J. Stenger, H.-J. Miesner, D. M. Stamper-Kurn, and W. Ketterle, "Observation of Feshbach resonances in a Bose-Einstein condensate," *Nature*, vol. 392, no. 6672, pp. 151–154, 1998. (cited on page 1)

[15] C. Chin, R. Grimm, P. Julienne, and E. Tiesinga, "Feshbach resonances in ultracold gases," *Rev. Mod. Phys.*, vol. 82, pp. 1225–1286, Apr 2010. (cited on pages 1 and 6)

[16] G. Gauthier, I. Lenton, N. M. Parry, M. Baker, M. J. Davis, H. Rubinsztein-Dunlop, and T. W. Neely, "Direct imaging of a digital-micromirror device for configurable microscopic optical potentials," *Optica*, vol. 3, no. 10, pp. 1136–1143, Oct 2016. (cited on pages 1 and 62)

[17] F. Schäfer, T. Fukuhara, S. Sugawa, Y. Takasu, and Y. Takahashi, "Tools for quantum simulation with ultracold atoms in optical lattices," *Nature Reviews Physics*, vol. 2, no. 8, p. 411–425, Jul. 2020. (cited on page 1)

[18] H. J. Metcalf and P. van der Straten, "Laser cooling and trapping of neutral atoms," Jul. 2007. (cited on pages 1, 4, 30, and 33)

[19] C. Baroni, G. Lamporesi, and M. Zaccanti, "Quantum mixtures of ultracold gases of neutral atoms," 2024. (cited on page 1)

[20] M. Schecter and A. Kamenev, "Phonon-mediated Casimir interaction between mobile impurities in one-dimensional quantum liquids," *Phys. Rev. Lett.*, vol. 112, p. 155301, Apr 2014. (cited on page 2)

[21] J. Tempere, W. Casteels, M. K. Oberthaler, S. Knoop, E. Timmermans, and J. T. Devreese, "Feynman path-integral treatment of the BEC-impurity polaron," *Phys. Rev. B*, vol. 80, p. 184504, Nov 2009. (cited on page 2)

[22] P. Naidon, "Two impurities in a Bose–Einstein condensate: From Yukawa to Efimov attracted polarons," *Journal of the Physical Society of Japan*, vol. 87, no. 4, p. 043002, 2018. (cited on page 2)

[23] B. Reichert, Z. Ristivojevic, and A. Petković, "The Casimir-like effect in a one-dimensional Bose gas," *New Journal of Physics*, vol. 21, no. 5, p. 053024, May 2019. (cited on page 2)

[24] V. P. Singh, L. Amico, and L. Mathey, "Thermal suppression of demixing dynamics in a binary condensate," *Phys. Rev. Res.*, vol. 5, p. 043042, Oct 2023. (cited on page 2)

[25] P. Ao and S. T. Chui, "Binary Bose-Einstein condensate mixtures in weakly and strongly segregated phases," *Phys. Rev. A*, vol. 58, pp. 4836–4840, Dec 1998. (cited on pages 2 and 6)

[26] D. S. Petrov, "Quantum mechanical stabilization of a collapsing Bose-Bose mixture," *Phys. Rev. Lett.*, vol. 115, p. 155302, Oct 2015. (cited on page 2)

[27] E. M. Gutierrez, G. A. de Oliveira, K. M. Farias, V. S. Bagnato, and P. C. M. Castilho, "Miscibility regimes in a 23Na–39K quantum mixture," *Applied Sciences*, vol. 11, no. 19, 2021. (cited on page 2)

[28] T. V. Zache, F. Hebenstreit, F. Jendrzejewski, M. K. Oberthaler, J. Berges, and P. Hauke, "Quantum simulation of lattice gauge theories using wilson fermions," *Quantum Science and Technology*, vol. 3, no. 3, p. 034010, Jun. 2018. (cited on page 2)

[29] A. Mil, T. V. Zache, A. Hegde, A. Xia, R. P. Bhatt, M. K. Oberthaler, P. Hauke, J. Berges, and F. Jendrzejewski, "A scalable realization of local U(1) gauge invariance in cold atomic mixtures," *Science*, vol. 367, no. 6482, pp. 1128–1130, 2020. (cited on page 2)

[30] J. Kilinc, "A new setup for experiments with an ultracold ^{23}Na-^{39}K mixture," Ph.D. dissertation, Universität Heidelberg, 2024. (cited on pages 3, 7, 9, 13, 14, 16, 19, 29, 30, 34, 36, 37, 38, 48, 49, and 59)

[31] L. Höcker, "Progress and challenges in setting up an ultracold ^{23}Na-^{39}K quantum gas experiment," Ph.D. dissertation, University Heidelberg, 2024. (cited on pages 3, 4, and 62)

[32] C. Pethick and H. Smith, *Bose-Einstein Condensation in Dilute Gases*. Cambridge University Press, 2002. (cited on page 4)

[33] F. Dalfovo, S. Giorgini, L. P. Pitaevskii, and S. Stringari, "Theory of Bose-Einstein condensation in trapped gases," *Rev. Mod. Phys.*, vol. 71, pp. 463–512, Apr 1999. (cited on page 4)

[34] L. Pitaevskii and S. Stringari, *Bose-Einstein Condensation*, ser. International Series of Monographs on Physics. Clarendon Press, 2003. (cited on pages 4, 6, and 7)

[35] W. Ketterle, D. Durfee, and D. M. Stamper-Kurn, "Making, probing and understanding Bose-Einstein condensates," *arXiv: Condensed Matter*, 1999. (cited on pages 4 and 49)

[36] A. Einstein, "Quantentheorie des einatomigen idealen gases," in *Sitzungsberichte der Preussischen Akademie der Wissenschaften XXII*, 1924, pp. 167–267. (cited on page 4)

[37] Bose, "Plancks gesetz und lichtquantenhypothese," *Zeitschrift für Physik*, vol. 26, no. 1, p. 178–181, Dec. 1924. (cited on page 4)

[38] E. P. Gross, "Structure of a quantized vortex in boson systems," *Il Nuovo Cimento (1955-1965)*, vol. 20, no. 3, pp. 454–477, 1961. (cited on page 5)

[39] L. P. Pitaevskii, "Vortex lines in an imperfect Bose gas," *Sov. Phys. JETP*, vol. 13, no. 2, p. 451, Aug. 1961. (cited on page 5)

[40] T. A. Schulze, T. Hartmann, K. K. Voges, M. W. Gempel, E. Tiemann, A. Zenesini, and S. Ospelkaus, "Feshbach spectroscopy and dual-species Bose-Einstein condensation of ^{23}Na$-^{39}$K mixtures," *Phys. Rev. A*, vol. 97, p. 023623, Feb 2018. (cited on pages 7 and 9)

[41] J. Dreher, "An offset locking scheme for absorption imaging of ^{39}K at high magnetic fields," Bachelor's Thesis, Universität Heidelberg, 2019. (cited on pages 9, 18, and 21)

[42] U. Schünemann, H. Engler, R. Grimm, M. Weidemüller, and M. Zielonkowski, "Simple scheme for tunable frequency offset locking of two lasers," *Review of Scientific Instruments*, vol. 70, pp. 242–243, 1 1999. (cited on page 9)

[43] W. Demtröder, *Experimentalphysik 3*, 5th ed., ser. Springer-Lehrbuch. Berlin, Germany: Springer, Jun. 2016. (cited on page 11)

[44] T. G. Tiecke, "Properties of potassium," 2011. (cited on pages 11 and 13)

[45] H. Haken and H. C. Wolf, *Atom- Und Quantenphysik*, 8th ed., ser. Springer-Lehrbuch. Berlin, Germany: Springer, Sep. 2003. (cited on page 11)

[46] E. Arimondo, M. Inguscio, and P. Violino, "Experimental determinations of the hyperfine structure in the alkali atoms," *Rev. Mod. Phys.*, vol. 49, pp. 31–75, Jan 1977. (cited on page 11)

[47] R. P. Feynman, R. B. Leighton, M. Sands, and R. B. Lindsay, "The feynman lectures on physics, vol. 3: Quantum mechanics," *Physics Today*, vol. 19, no. 11, Nov. 1966. (cited on page 12)

[48] G. Breit and I. I. Rabi, "Measurement of nuclear spin," *Phys. Rev.*, vol. 38, pp. 2082–2083, Dec 1931. (cited on page 12)

[49] M. Hans, "Physical computing on a versatile setup for ultra-cold potassium," Ph.D. dissertation, University Heidelberg, 2022. (cited on pages 15 and 62)

[50] Toptica application notes, "Error-signal generation," 2024. (cited on page 17)

[51] P. D. Lett, R. N. Watts, C. I. Westbrook, W. D. Phillips, P. L. Gould, and H. J. Metcalf, "Observation of atoms laser cooled below the doppler limit," *Phys. Rev. Lett.*, vol. 61, pp. 169–172, Jul 1988. (cited on page 30)

[52] J. Dalibard and C. Cohen-Tannoudji, "Laser cooling below the Doppler limit by polarization gradients: simple theoretical models," *J. Opt. Soc. Am. B*, vol. 6, no. 11, pp. 2023–2045, Nov 1989. (cited on pages 30, 31, and 32)

[53] A. Beikert, "Controlled frequency generation for grey molasses cooling," Bachelor's Thesis, University Heidelberg, 2021. (cited on pages 33 and 34)

[54] D. Steck, *Quantum and Atom Optics*, 2007. (cited on pages 33 and 36)

[55] M. Weidemüller, T. Esslinger, M. A. Ol'shanii, A. Hemmerich, and T. W. Hänsch, "A novel scheme for efficient cooling below the photon recoil limit," *Europhysics Letters (EPL)*, vol. 27, no. 2, p. 109–114, Jul. 1994. (cited on pages 34 and 35)

[56] C. Foot, *Atomic Physics*, ser. Oxford Master Series in Physics. OUP Oxford, 2005. (cited on pages 38 and 39)

[57] D. W. Preston, "Doppler-free saturated absorption: Laser spectroscopy," *American Journal of Physics*, vol. 64, no. 11, p. 1432–1436, Nov. 1996. (cited on page 39)

[58] W. Demtröder, *Laser Spectroscopy: Vol. 2: Experimental Techniques*. Springer Berlin Heidelberg, 2008. (cited on page 39)

[59] G. C. Bjorklund, M. D. Levenson, W. Lenth, and C. Ortiz, "Frequency modulation (fm) spectroscopy: Theory of lineshapes and signal-to-noise analysis," *Applied Physics B Photophysics and Laser Chemistry*, vol. 32, no. 3, p. 145–152, Nov. 1983. (cited on page 41)

[60] J. Kilinc, "Starting a Na-K experiment for simulating quantum many-body phenomena," Master's thesis, University Heidelberg, 2019. (cited on page 41)

[61] A. Weis and S. Derler, "Doppler modulation and zeeman modulation: laser frequency stabilization without direct frequency modulation," *Appl. Opt.*, vol. 27, no. 13, pp. 2662–2665, Jul 1988. (cited on page 41)

[62] D. Steck, "Sodium D line data," 2003. (cited on pages 44 and 52)

[63] H. K. Andersen, "Bose-einstein condensates in optical lattices," Ph.D. dissertation, University of Aarhus, 2008. (cited on page 49)

[64] S. Rosi, A. Burchianti, S. Conclave, D. S. Naik, G. Roati, C. Fort, and F. Minardi, "-enhanced grey molasses on the d2 transition of rubidium-87 atoms," *Scientific Reports*, vol. 8, no. 1, Jan. 2018. (cited on page 51)

[65] C. Heintze, "Projection of repulsive potentials in ultracold quantum gases with a digital micromirror device," Master's thesis, Universität Heidelberg, 2020. (cited on page 62)

Acknowledgements

I want to thank Markus for introducing me to quantum science, for recruiting me after an exciting seminar, and for always appreciating my contributions to the experiment.

Thank you Helmut, for always finding time for my little problems. It is incredible to me how you seem to be available for everything all the time and how quickly you can understand and oftentimes fix issues.

I want to thank Lauriane for agreeing to be a second examiner for my thesis. It is inspiring to me to see another woman succeed in a field that is very much still dominated by men. I wish you continued success in your academic journey.

The SoPa experiment would not be where it is today without the efforts of Jan and Lilo. It is incredible how much you two rebuilt in such a short amount of time. Thank you for teaching us about your experiment and being available in very stressful phases of your own degrees. Thank you, Jan for still caring so much about my progress, even though you were already on your way out. Thank you, Lilo for swimming and gardening lessons and for encouraging me to apply for the OPTO conference.

A special thanks goes out to my partners in crime Brian and Toni. Thank you Brian, for advancing this experiment so tirelessly. Thank you for offering an open ear for my personal issues and for encouraging me to find my passion, wherever that may lead me. Thanks, Toni for being the bridge between the different generations of the experiment. Thank you for being so involved with the experiment software and helping out with my software issues whenever they came up.

I also want to thank all the lovely other people who are part of the BECK, BEC, ArTTA, SpectER, and Grasenzer group. Thank you for all the fun breakfasts, Kranzmittwochs, defenses, and the retreat. Science can be exhausting, but it can also be so much fun, especially when there are people like you around.

Thanks Petra and thanks Christiane for all the administrative work you do for the group that you are always so wonderfully on top of. It is an unfortunate tendency that

administrators may get overlooked when they are so competent that everything runs smoothly. I hope you guys know, how much we all appreciate you.

Last but not least, I want to thank the people outside of the working group, some of whom were just as important in helping me finish this degree.

I want to thank Nico, for constantly, tirelessly building me up. For all the times you listened, paid attention, greeted me with cooked dinners and calming cups of tea. You were my rock.

I also want to thank Kai, Jonas, Nico, Brian, Lilo, and my dad for proofreading my thesis. Your criticisms thoroughly improved my work.

Thanks Lena, Lina, Jonas, Kai, Ana, Anton, Stani, Laurin, Philipp, Selina, Finn, Tobi, Elias, Emmy, Anna, Gabriel, Ben, Lucas, Niklas, and Bertram for being by my side during the Bachelor's and Master's degrees. The prospect of leaving Heidelberg is exciting but daunting. I will miss you guys. I will always cherish the fun we had together, the times we struggled together, the vacations we went on together and the days we just gammeled on the Neckarwiese.

And finally I want to thank my family. You have always taught me that curiosity is my biggest strength. Maybe one day I will be as assertive and educated as you Mom, as tech-savvy as you Nathan, and as established as a physicist as you, Dad. A girl can dream.

Erklärung

Ich versichere, dass ich diese Arbeit selbstständig verfasst und keine anderen als die angegebenen Quellen und Hilfsmittel benutzt habe.

Heidelberg, den 01.11.2024,

Malaika Göritz